# SANDIA REPORT

SAND2013-7201
Unlimited Release
Printed September 2013

# Z-Petawatt Driven Ion Beam Radiography Development

## LDRD 151367

Marius S. Schollmeier, Adam B. Sefkow, Matthias Geissel, Patrick K. Rambo,
and Jens Schwarz

Prepared by
Sandia National Laboratories
Albuquerque, New Mexico 87185 and Livermore, California 94550

Issued by Sandia National Laboratories, operated for the United States Department of Energy by Sandia Corporation.

Printed in the United States of America. This report has been reproduced directly from the best available copy.

Available to DOE and DOE contractors from
U.S. Department of Energy
Office of Scientific and Technical Information
P.O. Box 62
Oak Ridge, TN 37831

| | |
|---|---|
| Telephone: | (865) 576-8401 |
| Facsimile: | (865) 576-5728 |
| E-Mail: | reports@adonis.osti.gov |
| Online ordering: | http://www.osti.gov/bridge |

Available to the public from
U.S. Department of Commerce
National Technical Information Service
5285 Port Royal Rd.
Springfield, VA 22161

| | |
|---|---|
| Telephone: | (800) 553-6847 |
| Facsimile: | (703) 605-6900 |
| E-Mail: | orders@ntis.fedworld.gov |
| Online order: | http://www.ntis.gov/help/ordermethods.asp?loc=7-4-0#online |

SAND2013-7201
Unlimited Release
Printed September 2013

# Z-PETAWATT DRIVEN ION BEAM RADIOGRAPHY DEVELOPMENT

Marius S. Schollmeier, Matthias Geissel, Patrick K. Rambo, and Jens Schwarz
Laser Operations and Engineering Department

Adam B. Sefkow
ICF Target Design Department

Sandia National Laboratories
P.O. Box 5800
Albuquerque, New Mexico 87185-MS1193

## Abstract

Laser-driven proton radiography provides electromagnetic field mapping with high spatiotemporal resolution, and has been applied to many laser-driven High Energy Density Physics (HEDP) experiments. Our report addresses key questions about the feasibility of ion radiography at the Z-Accelerator ("Z"), concerning laser configuration, hardware, and radiation background. Charged particle tracking revealed that radiography at Z requires GeV scale protons, which is out of reach for existing and near-future laser systems. However, it might be possible to perform proton deflectometry to detect magnetic flux compression in the fringe field region of a magnetized liner inertial fusion experiment. Experiments with the Z-Petawatt laser to enhance proton yield and energy showed an unexpected scaling with target thickness. Full-scale, 3D radiation-hydrodynamics simulations, coupled to fully explicit and kinetic 2D particle-in-cell simulations running for over 10 ps, explain the scaling by a complex interplay of laser prepulse, preplasma, and ps-scale temporal rising edge of the laser.

# ACKNOWLEDGMENTS

A.B.S. acknowledges S.E. Corwell, K.M. Lord, the TLCC and TLCC2 teams at Sandia, and D. R. Welch for simulation support. The authors acknowledge B.W. Atherton, R.D. McBride, M.C. Herrmann, C.W. Nakhleh, J.L. Porter and Org. 01682 at Sandia for support, A.V. Arefiev and B.N. Breizman at UT Austin, K.A. Flippo and the TRIDENT laser facility staff at Los Alamos National Laboratory, as well as S.A. Gaillard and D.T. Offermann.

# CONTENTS

# FIGURES

# NOMENCLATURE

| | |
|---|---|
| CAD | Computer-Aided Design |
| DOE | Department of Energy |
| EPM | Ellipsoidal Plasma Mirror |
| FOA | Final Optics Assembly |
| FWHM | Full-Width-at-Half-Maximum |
| HEDP | High Energy Density Physics |
| ICF | Inertial Confinement Fusion |
| IP | Image Plate |
| LANL | Los Alamos National Laboratory |
| LDRD | Laboratory Directed Research & Development |
| LF | Large area foil |
| LSP | Large Scale Plasma simulation code |
| MA | Mega-Ampere |
| MeV | Mega-Electronvolt |
| MLT | Mass-limited target |
| OAP | Off-Axis Parabolic mirror |
| PIC | Particle-in-cell code |
| PM | Plasma Mirror |
| PW | Petawatt |
| RCF | RadioChromic Film |
| SNL | Sandia National Laboratories |
| TNSA | Target Normal Sheath Acceleration |
| Z | Z-Accelerator at SNL |
| ZPW | Z-Petawatt Laser at SNL |

This page intentionally left blank.

# 1. INTRODUCTION

The capability to image a transient state adds significantly to the understanding of various scientific experiments. Sometimes such images are critical components of science and engineering research. Within the fields of Inertial Confinement Fusion (ICF) and High Energy Density Physics (HEDP) research at Sandia's Z-Accelerator ("Z"), x-ray backlit imaging [1] creates stunning snapshots of the target during a Megajoule-driven discharge of Z. Intensity contrast in the image is generated because the x-rays are attenuated with increasing line density of the target. Thus, x-ray backlighting is mainly sensitive to the density distribution of the target. However, the MA, ns-current of Z generates very strong magnetic as well as electric fields. Imaging those fields would add significantly to the physics understanding of the experiment. Charged particles such as electrons or ions are sensitive to electromagnetic (EM) fields. Hence charged particle beams can be used for radiographing those fields.

Proton radiography for hydrodynamics and weapons physics has been previously developed using beams from conventional particle accelerators [2]. Here, ~200 MeV to GeV protons are used to radiograph thick and dense objects. While it is not feasible to build a 100-MeV-class ion accelerator such as a synchrotron next to Z, it is possible to use the Z-Petawatt (ZPW) shortpulse laser instead. Shortpulse lasers, when focused onto µm-thick metal foils, generate proton and heavy ion beams with tens of MeV energy. With great success, laser-driven protons have been applied as a diagnostic for transient electromagnetic fields in laser-plasma interactions [3]. Due to the small source size, laser-driven proton beam radiography is similar to point-projection imaging by x-rays but with the added benefit that it is sensitive to EM fields. To-date, laser-driven proton radiography has only been applied to laser-driven HEDP experiments. This LDRD project intended to extend laser-driven ion radiography to the MJ pulsed power machine Z. The generation of protons or heavy ions with MeV energies from a laser target foil inside Z's vacuum center section would enable ion radiography or deflectometry of an ion pencil beam to diagnose Z's electromagnetic field structures with micron-scale spatial and ps-scale temporal resolution. This would allow unmatched insights into both the target performance for e.g. spherical capsule implosions, magnetic flux compression or astrophysical jet simulations, as well as the machine performance.

## 1.1. ION ACCELERATION WITH SHORTPULSE LASERS

In the early 2000's it was found that an intense (intensity $I > 10^{18}$ W/cm$^2$) laser pulse irradiating a thin, solid-density target generates collimated, MeV proton beams [4-6]. Although the laser pulse is very intense, direct laser-ion acceleration is strictly speaking not happening. Charged particles interact with the laser field according to the Lorentz force:

$$\frac{d\boldsymbol{p}}{dt} = \frac{Zq}{m}(\boldsymbol{E} + \boldsymbol{v} \times \boldsymbol{B}), \tag{1}$$

where $\boldsymbol{p}$ denotes the particle momentum vector, $Z$ its nuclear charge state, $q$ the elementary charge, $m$ the particle mass, $\boldsymbol{v}$ the particle velocity vector, $\boldsymbol{E}$ the electric field and $\boldsymbol{B}$ the magnetic field vectors of the laser wave, respectively.

For non-relativistic velocities $v \ll c$ the force acting on a charged particle is given by the electric field only. The solution of the equation of motion leads to a harmonic oscillation with the amplitude or quiver velocity

$$v_{osc} = \frac{qE}{m\omega_L}. \quad (2)$$

$\omega_L$ is the laser angular frequency. In a non-relativistic treatment, $v_{osc}$ becomes c when the electric field amplitude $E_0 = 3.2 \times 10^{12}$ V/m, that is for intensities $I = 1.37 \times 10^{18}$ W/cm$^2$. Hence laser-electron interaction is called relativistic if the dimensionless electric field amplitude

$$a_0 = \frac{qE}{m\omega_L c} = \sqrt{\frac{I_0\left[\frac{W}{cm^2}\right]\lambda^2[\mu m^2]}{1.37 \times 10^{18}}} > 1, \quad (3)$$

where $I_0$ is the laser intensity in W/cm$^2$, and $\lambda$ the laser wavelength. For protons, the intensity needs to be $I > 5 \times 10^{24}$ W/cm$^2$, which is beyond reach of present laser systems.

The laser interacts with the electrons, e.g., at the critical density where it gets reflected the laser pushes the electrons by the ponderomotive force [7]. The electrons then interact with the remaining ions via the electric force due to charge-separation. The fields created in this manner can be as high as the laser field itself. Since the ion motion is about a factor of $(m_i/Z_i m_e)^{1/2}$ slower, the field remains stationary for relatively long times compared to the laser oscillation. The ions can gain energy by the potential of this field; their energy is equal to the ponderomotive potential. The ions start to blow-off and can gain energy on the order of a few MeV [8].

In laser-matter interaction a variety of ion-acceleration schemes were identified, e.g., long-pulse (nanosecond) plasma thermal expansion [8], Coulomb explosion of laser-irradiated clusters [9], transverse acceleration in underdense plasma channels [10], ion acceleration in a charge-separation field by a quasi-stationary magnetic field [11] or acceleration from the shock front induced by laser hole boring [12]. Low-energy, but high-current ion beams can be produced by the skin-layer ponderomotive acceleration [13] with sub-relativistic intensities.

Theoretical studies have identified a very efficient acceleration of ultra-thin (nm-sized) foils by circularly polarized, ultra-high contrast laser radiation [14]. For linear polarization and ultra-high contrast as well, the irradiation of a nm-thin foil can lead to GeV energies by the laser-breakout afterburner effect [15]. Future generations of high-energy, high-intensity lasers with $I_L > 1.37 \times 10^{23}$ W/cm$^2$ and ultra-high contrast might be able to enter the laser-piston acceleration regime. Here, the radiation pressure can directly accelerate ions to GeV energies [16].

The scope of this LDRD project was on the ion acceleration process that is the most efficient in terms of beam quality and usability to date: the acceleration of ions from the rear, i.e., the non-irradiated sides of thin foil targets. The principal mechanism was quantitatively explained by Scott Wilks *et al.* [17] and is known since then as the target normal sheath acceleration (TNSA).

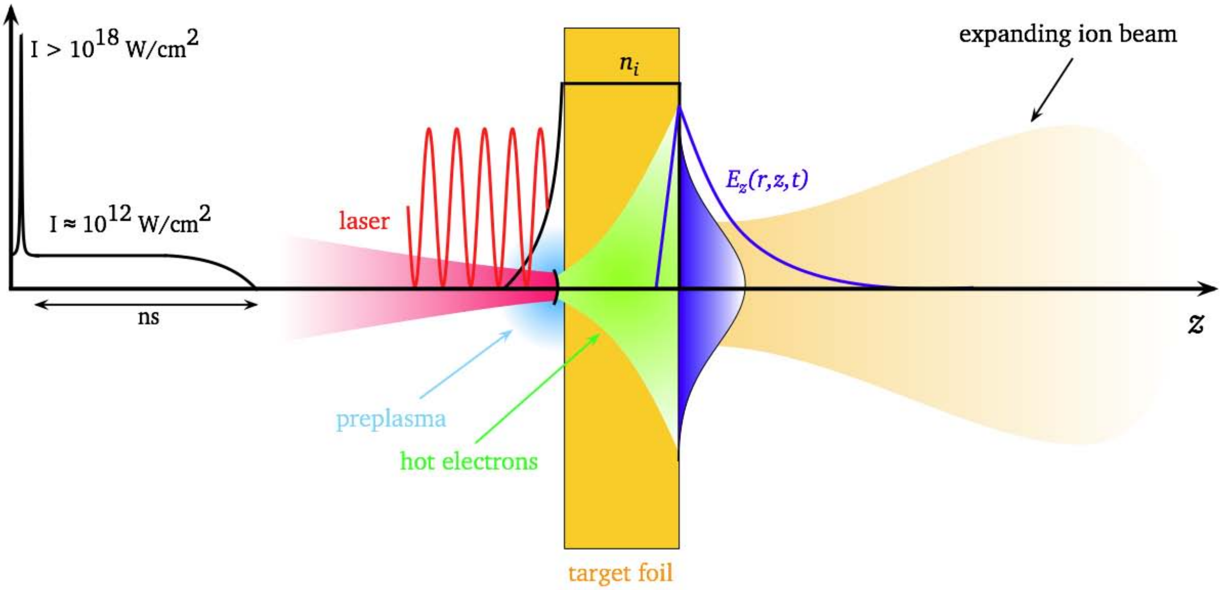

**Figure 1: Schematic of Target Normal Sheath Accelation (TNSA).** *A thin target foil is irradiated by an intense laser pulse. The laser prepulse creates a preplasma on the target's front side. The main pulse interacts with the plasma and accelerates MeV-energy electrons in forward direction (a schematic lineout of the ion density $n_i$ is represented by the black line). The electrons propagate through the target and leave the rear side, where they set up a dense sheath. The electric field $E_z(r,z,t)$ of the sheath is on the order of MV/µm, sufficient to ionize atoms at the surface. The ions are then accelerated in this sheath field, pointing in the target normal direction.*

A schematic of the acceleration process is shown in Figure 1. The preceding pedestal of the laser (the prepulse) with intensity on the order of $10^{-6}$-fold the main pulse intensity creates a preplasma at the target's front side. Prepulses can be created by amplified spontaneous emission (ASE) as well as spectral modulations in the process of chirped-pulse amplification and compression. The main pulse then interacts with the plasma, accelerating electrons that are directed mainly in forward direction. The electrons propagate through the foil; collisions with the background material can increase the initial divergence of the electron flow. The electrons then leave the rear side, forming a dense electron cloud. The charge separation of the electrons from the remaining target creates a strong electric field on the order of MV/µm within a thin sheath. The field ionizes atoms at the rear side, i.e., protons and carbon ions from contamination layers. The ions are then accelerated along the target normal direction, gaining energies up to tens of MeV.

### 1.1.1 *Proton Beam Properties*

Here we briefly summarize the key features of laser-accelerated proton beams. A more detailed summary can be found in Ref. [18]. Figure 2 shows some typical results for beams generated with ZPW and with Trident at Los Alamos National Laboratory (LANL). Both laser systems generate short laser pulses of ≈1054 nm, ≈100 J energy, 500 fs duration and more than $10^{20}$ W/cm$^2$ on target.

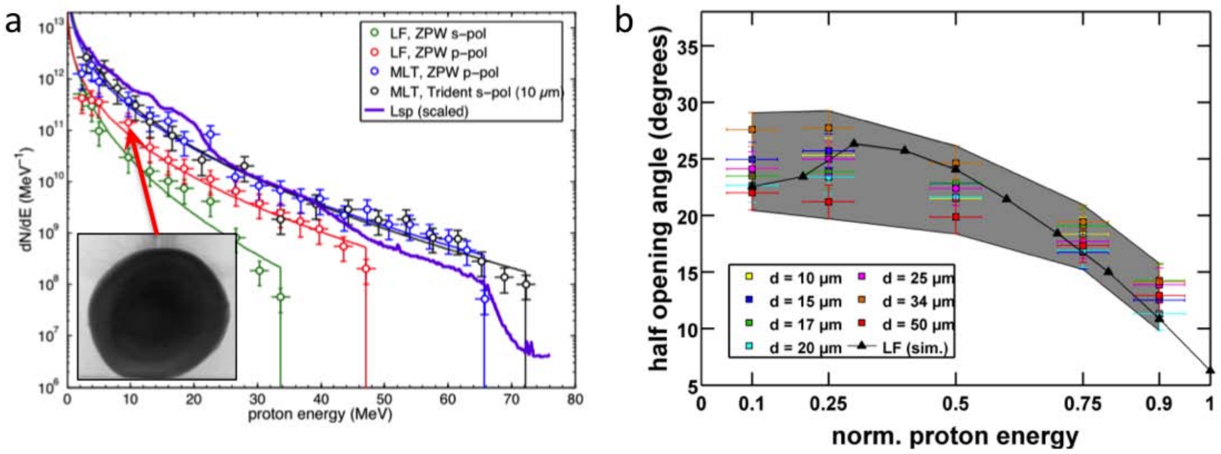

**Figure 2: Properties of laser-accelerated proton beams.** *a) typical spectra measured at ZPW and at Trident (LANL). The inset shows a 10 MeV beam profile for a LF target. b) beam envelope half opening angle vs. normalized proton energy. Each data set was normalized to its respective maximum energy for a better comparison.*

The main plot (Figure 2a) presents proton spectra for two different target types: Large area foils (LF) with transverse dimensions of several mm, as well as mass-limited targets (MLT). MLT have transverse dimensions shorter than the distance a relativistic electron can propagate within the laser pulse duration. For example, for a 1 ps laser pulse the size should be smaller than $c \times 1$ ps = 300 µm. The spectra are exponentially decaying; there is a sharp cutoff at the maximum energy. The inset shows a 10 MeV beam profile, measured with Ashland GAFCHROMIC[1] self-developing HD radiochromic film[2] (RCF). The beam is smooth and round, with only little modulations in the center. The particle count per MeV ranges from $10^{12}$ for ≈ 1 MeV protons to $10^{6}$ for protons with tens of MeV. Figure 2b presents the beam divergence vs. energy. Plotted is the envelope half opening angle vs. normalized energy. Each data set was normalized to its respective maximum energy for a better comparison. The beams are divergent with an energy-dependent envelope angle [18,19]. Lower energy protons are less collimated (about 30° half-angle) than higher energy protons (about 5°). The black line represents simulation data for ZPW, which will be further described in section 5. Furthermore, the beams have a very small emittance [18,20]. Thus they are very laminar, which in combination with the large divergence permits their use in point-projection imaging with µm-scale spatial resolution.

Figure 3 presents the scaling of the maximum energy with laser intensity for different laser systems. The grey, horizontal line marks 60 MeV, which is an empirically found barrier [21] that could not be overcome since the very first measurements at NOVA Petawatt [6]. The data can be broadly fit with a scaling law [22] that is based on a one-dimensional, isothermal plasma expansion model. Using so-called mass-limited targets (see section 4.4 for details) we could overcome this barrier during this LDRD project. However, the gain in energy was only small (i.e., from 50 to 65 MeV at ZPW and from 50 to 75 MeV at Trident), and it was not very reproducible. The scaling law suggests that an irradiance above $10^{21}$ W/cm$^{2}$ for a 1 ps pulse laser

---

[1] GAFCHROMIC® is a registered trademark of Ashland, Inc.

[2] http://www.ashland.com/products/gafchromic-radiotherapy-films

is required. This requires almost a kJ of laser energy. A pulse of this energy might change the laser-target interaction and the fit with a scaling law. Indications for a different scaling (using a somewhat longer pulse duration of 10 ps) for kJ-class shortpulse lasers have been published by Offermann *et al.* [23].

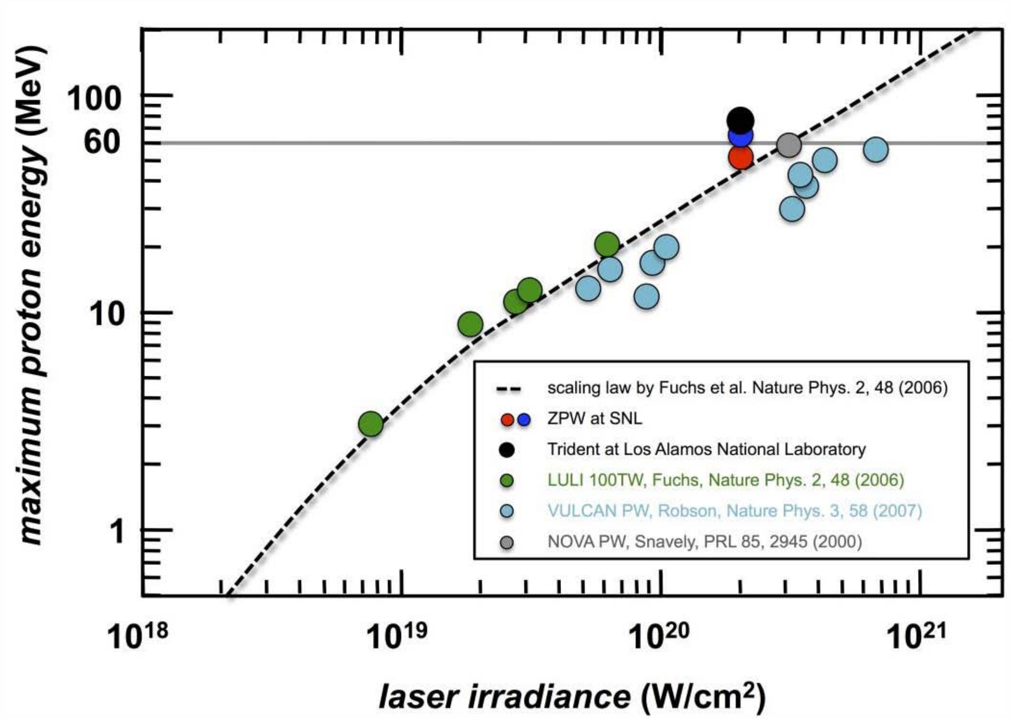

**Figure 3: Scaling of the maximum proton energy with laser intensity.** *Data points were taken from Refs. [22] (green circles), [24] (cyan circles), and [6] (grey circle), respectively. During this LDRD, we obtained 50 MeV (red circle) with large foil targets and 65 MeV (red circle) with mass-limited targets at ZPW; at Trident (LANL) we measured up to 75 MeV (black circle). The grey, horizontal line represents the empirical 60 MeV threshold [21].*

## 1.2. LASER-DRIVEN PROTON RADIOGRAPHY

The unique properties of laser-accelerated protons are favorable for achieving high spatial resolution with some magnification, when back illuminating an object with the proton beam via point-projection imaging scheme. Figure 4a shows a cartoon of the experimental set-up. The object to be radiographed is placed a short distance behind the source. The divergent proton beam is measured with a stack of RCF. The stack measures the protons at discrete energy intervals, which allows for time resolution via Time-of-Flight measurements. The source emission duration is on the order of a ps. The wide energy spread of the proton beam corresponds to a wide velocity spread, which results in a temporal spread to about ns duration shortly behind the source. The proton beam is velocity-chirped, similar to a frequency-chirped laser beam. Figure 4b shows typical response functions of RCF to protons with a broad energy range. The response functions exhibit a sharp peak, which means they are mainly sensitive to only a small energy interval (≈ 0.5 MeV). This adds an important benefit for radiography: each

RCF image is nearly monochromatic, and thus corresponds to a brief instant in time (ps scale). A complete RCF stack can thus cover a ns-duration time window with ps time resolution!

Proton projection imaging [25] has been developed during the past few years, in which electric and magnetic fields are detected via the local deflections undergone by a diverging beam of laser-accelerated protons. This approach has been shown to be particularly suited to the investigation of the dynamics of transient fields (i.e. varying on ps timescales) [26-32]. EM-field distributions can cause proton density modulations and trajectory intersections, which appear as caustics. Particle tracking codes, which follow the propagation of the protons through a given three-dimensional field structure, can retrieve the field distributions from the measured data.

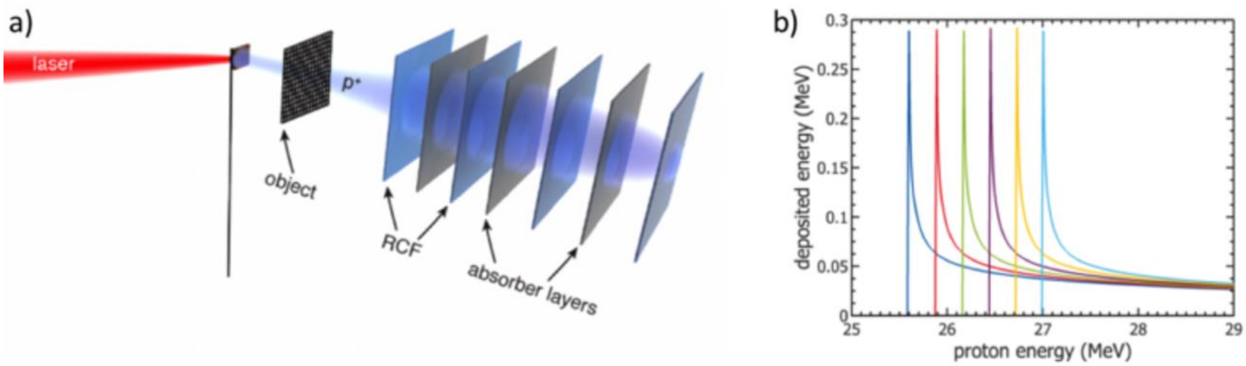

**Figure 4: Cartoon of laser-driven proton radiography.** *a) The object to be radiographed is placed a short distance behind the source. Protons propagate through the object and are measured with a stack of RCF in a few cm distance. The divergent proton beam creates a magnified image. Each RCF records mainly within a small energy interval, as shown by the response functions in b). Here, each color represents the reponse function for a different RCF.*

Alternatively, thin meshes inserted in the beam, e.g., between the proton source and the object are sometimes used as “markers” for the different parts of the proton beam cross sections, in a proper proton deflectometry arrangement [23,28,33-37]. Proton deflectometry has been used to diagnose the electromagnetic fields of a laser-driven, single wire Z-pinch [38]. In their conclusions, the authors suggest to apply proton deflectometry at Z. Another laser-driven experiment used proton deflectometry to measure magnetic flux compression [39], similar to the Magnetized Liner Inertial Fusion (MagLIF) experiments [40] being performed at Z.
An image of a 230 lines-per-inch mesh (8.6 μm wires, 110 μm period), generated with ZPW, is shown in Figure 5. The mesh was placed 3 mm behind the source. Even after 11 cm of propagation the imprint of the mesh is still clear and crisp, demonstrating the low emittance and high spatial resolution.

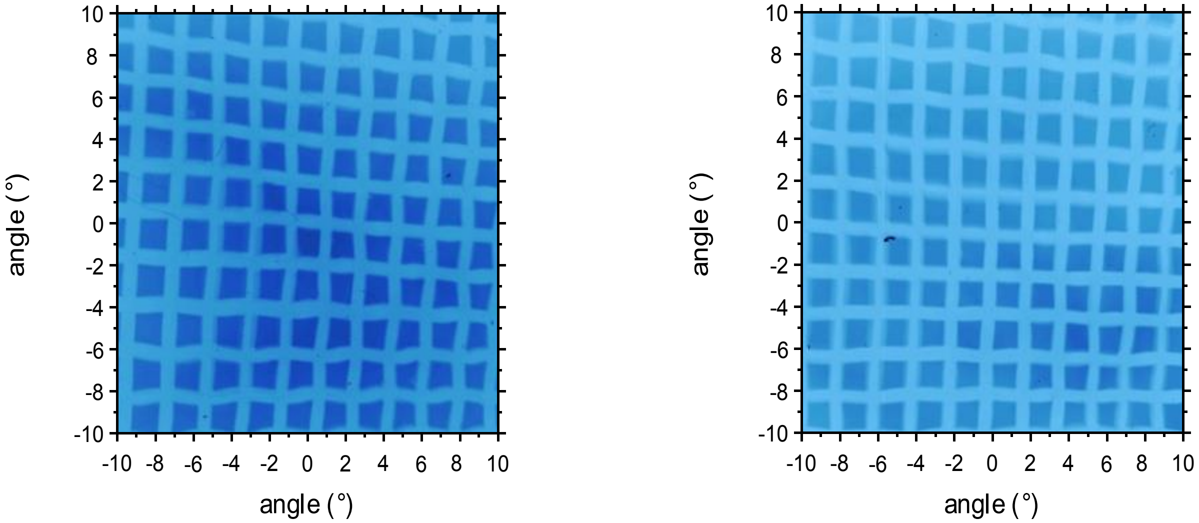

**Figure 5: Mesh imprint for 8 MeV protons after 3 cm (left) and 11 cm (right) propagation.**

## 1.3. CONSIDERATIONS FOR ION BEAM GENERATION AT Z

Unlike laser target chambers, the vacuum center section of Z is tightly packed not only with diagnostics but also with substantial debris mitigation measures. Access for a high-energy laser beam can only be made from the top. Figure 6 shows a CAD drawing of the ZPW Final Optics Assembly (FOA). To protect the expensive, long-lead-time focusing parabola from damage by debris many different protection devices have been implemented [41]. The ZPW laser pulse enters the experiment ("Z pinch") through a hole in the blast shield. A zoomed view of Z's center, without the blast shield, is shown in Figure 7a. The laser irradiates a small target to generate high-energy x-rays for point-projection imaging. Cameras are used to align the target and the laser.

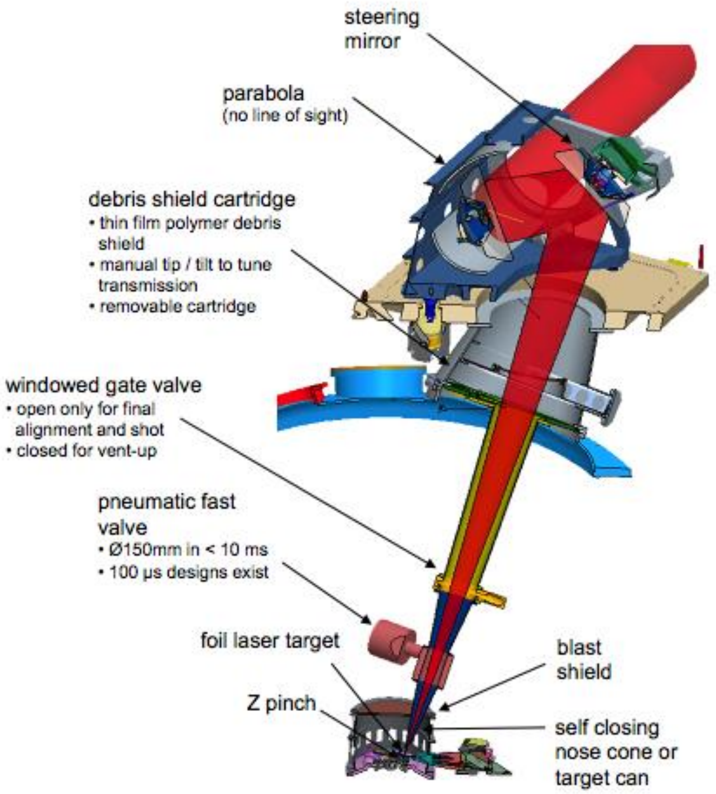

**Figure 6: Final Optics Assembly (FOA) for ZPW at Z.** *Image courtesy of Marc Ramsey (SNL).*

This configuration would have to be modified for ion acceleration, as the laser beam needs to be re-directed close to the target to enable ion acceleration in horizontal direction. Beam re-direction can be done with plasma mirrors (PM) [42]. We have tested and verified PM operation with ZPW shortly before this LDRD project started [43]. Figure 7b shows a proposed ZPW focusing modification. Instead of a flat PM, one could use an ellipsoidal plasma mirror (EPM) [44,45] to simultaneously re-direct the laser beam, increase the laser intensity and decrease pointing fluctuations. EPM are characterized by having two foci. ZPW can be focused to the first focal spot of the EPM, and the mirror will image this focus to the second focal spot. By properly choosing the incidence angle and aspect ratio of the ellipsoid [45], a de-magnification of the focal spot can be obtained. EPM development in the framework of this LDRD will be described in section 2.1.

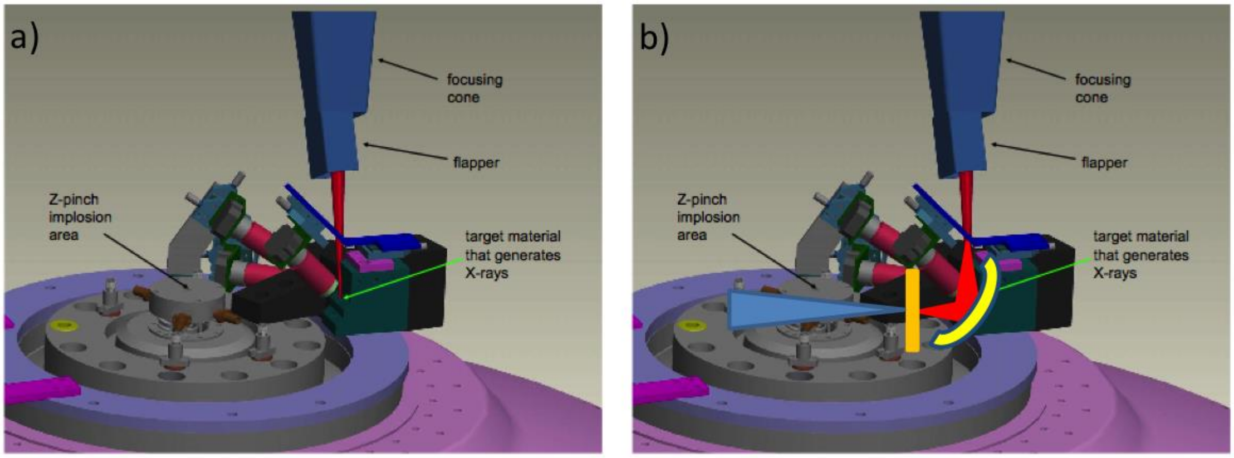

**Figure 7: Zoomed view of Z's center section without blast shield.** *a) target box and alignment cameras for an x-ray point-projection experiment. ZPW's laser pulse enters from the top to irradiate the target. b) proposed modification to re-direct the beam close to Z's center with a plasma mirror to enable near-normal irradiation of a target for ion acceleration.*

## 1.4. SCIENCE GOALS

Our research project attempts to answer the following key questions:

- What is needed to generate an ion beam at Z? What are the hardware requirements?
- The proton energy record at project begin was ≈60 MeV, using 500J/500fs PW lasers [6,24]. Is that good enough for Z?
- The most interested customer is the MagLIF project. Is proton radiography feasible to detect magnetic flux compression for MagLIF?
- Is radiation background at Z an issue for the planned detector?
- How can one improve laser-driven ion acceleration for better signal-to-noise ratio, shot-to-shot repeatability, higher cutoff energies, better beam collimation, etc.

The following section will describe the research performed to answer these questions.

# 2. DIAGNOSTICS REQUIREMENTS AT Z

## 2.1. ELLIPSOIDAL PLASMA MIRRORS

As mentioned in section 1.3, ZPW needs to be re-directed close to the target to enable ion acceleration in horizontal direction for proton radiography or deflectometry. The current FOA contains an $\mathrm{F}/\# = 11$ parabolic mirror with $\mathrm{f} = 4.73$ m focal length. The diffraction limited Airy spot has a radius of $\mathrm{r} = 1.22 \times \lambda\mathrm{F} = 14\ \mu\mathrm{m}$ (maximum to first minimum). Assuming 500 J energy in a 500 fs pulse, and 50% of the energy within the Airy spot, the diffraction limited intensity is $\mathrm{I} = 8 \times 10^{19}\ \mathrm{W/cm^2}$. According to Figure 3 the proton cutoff energy to be expected is ≈30-40 MeV. This will be even lower when a flat PM will be used, since PM's only reflect about 30-80% of the beam energy [43]. Depending on the radiography requirements these proton energies might be too low.

EPMs promise to provide a solution to this problem. Figure 8 shows the operating principle of an EPM. ZPW is focused to the first focal spot of the ellipsoid. The EPM images this spot to the second focal spot where the target is placed. Depending on the incidence angle of ZPW, the 2nd focal spot is much closer to the EPM than the first, which results in beam de-magnification. A de-magnification of the beam focus also means that pointing fluctuations of the laser beam are reduced by the same amount. This is important for an application at Z since the beam pointing fluctuations are substantial. Additionally, an aperture could be placed at the first focus to further enhance the debris protection.

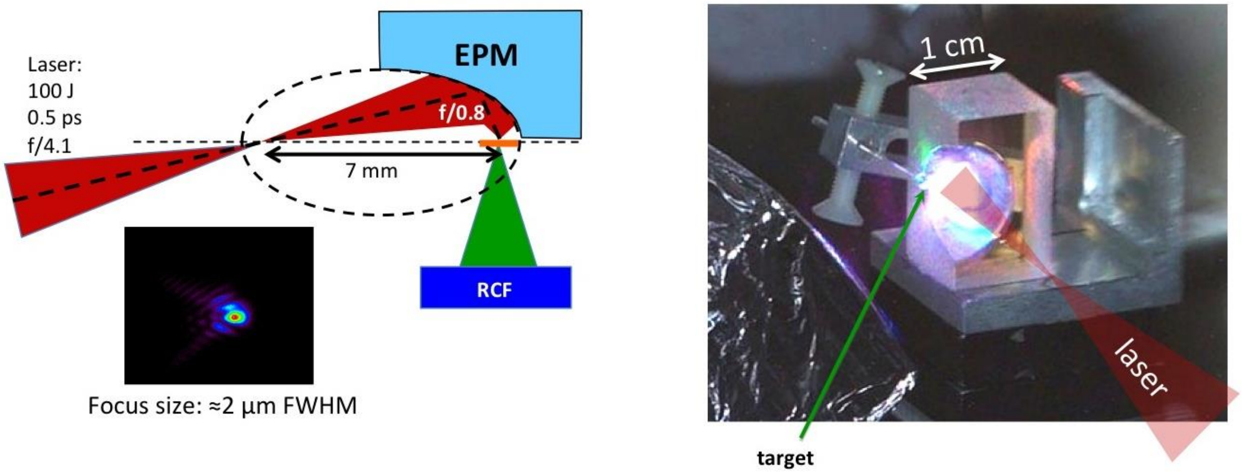

**Figure 8: Operating principle of an ellipsoidal plasma mirror.** *ZPW is focused to the first focal spot of the ellipsoid. The EPM images this spot to the second focal spot. Depending on the incidence angle of ZPW, the 2nd focal spot is much closer to the EPM than the first, which results in beam de-magnification. A focal spot size of 2 µm FWHM was obtained in test experiments at ZPW. The right image shows a photograph of the 1 cm glass EPM prototypes used [M. Nakatsutsumi* et al.*, unpublished].*

Prior to this LDRD project test experiments with colleagues from Ecole Polytechnique (France) and Osaka University (Japan) were done at the 100 TW target chamber of ZPW. A focal spot size of ≈ 2 µm FWHM was obtained (cf., the regular spot size is ≈ 6 µm FWHM). The right side of Figure 8 shows a photograph of the ≈1 $cm^3$ glass EPM prototype. Using a 50 x 50 x 1 $\mu m^3$ Al target, the maximum proton energy was 45 MeV. In contrast, using a flat PM resulted in 25 MeV. Thus, the EPM recovered the result obtained by direct irradiation (see Figure 2a). The main drawback of these EPM prototypes was that they did not have any alignment markers. EPM need to be replaced after a laser shot; the prototypes required very elaborate alignment, which took over 2 hours per mirror.

### 2.1.1 *“Alignment-free” EPM Prototype*

Such time-consuming alignment procedures are not acceptable for an application at Z. We have started to develop an “alignment-free” EPM. The main idea is to design an EPM with built-in alignment features that allow to quickly align the EPM initially and to replace it after the shot without major re-alignment. Quick replacement will not be important for Z experiments, but for offline experiments using only ZPW.

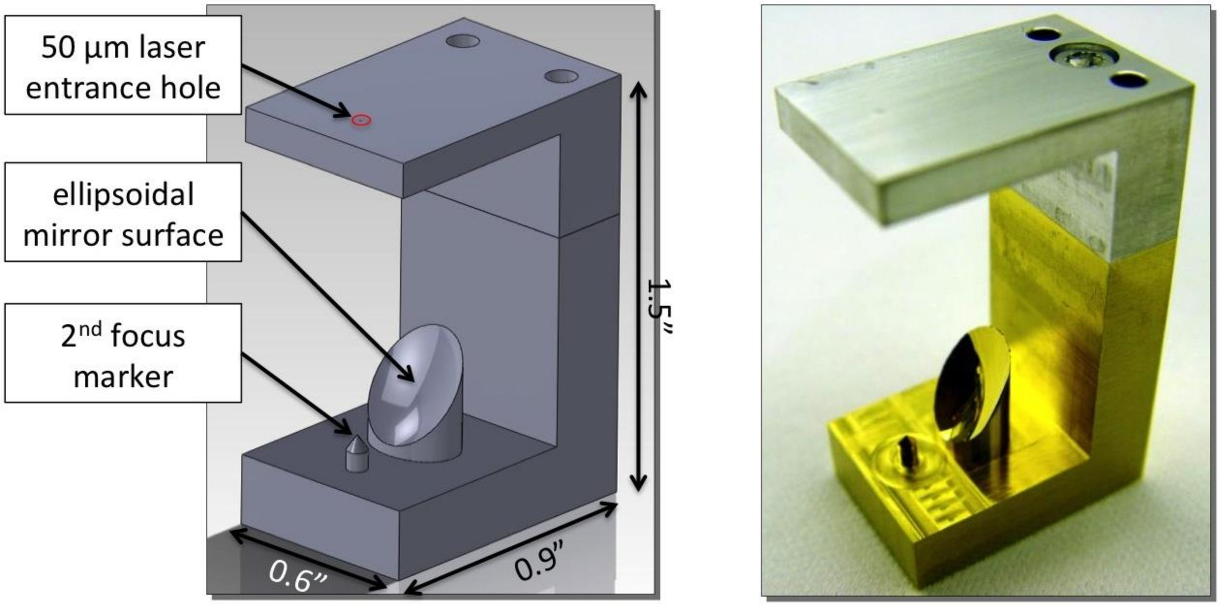

SolidWorks model

Alignment Ellipsoid: S/N 111205P02

**Figure 9: EPM prototype with built-in alignment features.**

The “alignment-free” EPM was designed by Raytheon Ktech’s Materials Processing and Coatings Lab (MPCL) according to Sandia’s specifications. Figure 9 shows the final prototype design. It was designed for a 4× demagnification. In contrast to the glass prototypes, the new EPM has built-in datum surfaces at the bottom, rear, and left side of the drawing and are diamond turned. The datum surfaces are reference to the EPM surface, and are precise within 10 µm which is the machine precision of the diamond lathe. Additionally, the top surface has a 50 µm diameter, 25 µm thick laser entrance hole (LEH) at the first focus position and a sharp, 50 µm size tip at the 2nd focus. The reflective area of the EPM was designed to be about 1 mm larger in radius than the laser beam, which will help with the alignment.

The EPM is mounted in a SNL-designed kinematic holder, where it rests on stainless steel balls on each datum surface and is held in place with magnets. In order for the magnets to hold the EPM in place, small pieces of Ni were glued onto the datum surface at the magnet positions. Figure 10 shows a CAD drawing of the holder.

The alignment procedure is as follows: Once the laser has been focused through the LEH, the EPM is turned and tilted until it homogeneously illuminates the EPM. This automatically leads to a second focus very near the pin. After that, only fine-tuning is needed for the final alignment.

The "shot" EPM will look very similar to the alignment EPM, but they will not have the grey-colored top piece and no pin at the 2nd focus to leave room for the target. After the shot, the EPM can be easily replaced with a new EPM.

A 5.7″×5.7″, 6-axis goniometer was acquired from Newport Corporation (Model no. 8095) to align the EPM inside the vacuum target chamber. The goniometer is shown in Figure 10 as well. The goniometer is motorized by Picomotor[3] actuators, which allow remote high-resolution (<30 nm) adjustment of various combinations of
Θ Θ Θ.

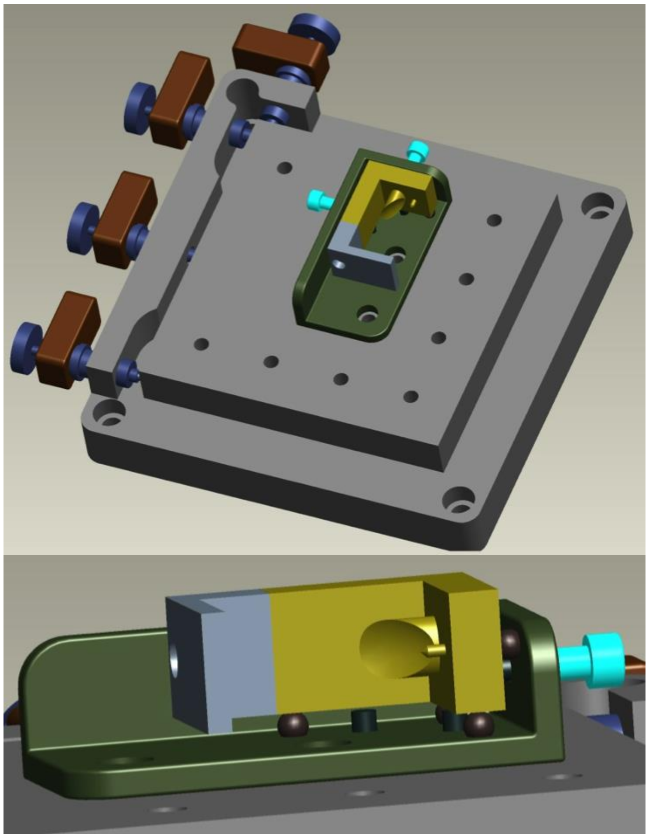

**Figure 10: EPM in kinematic holder, mounted to the 6-axis stage.**

## 2.1.2. EPM Motion Control Software

The necessity to drive more than one Picomotor simultaneously required developing motion control software. Furthermore, some motors serve multiple functions to translate, rotate or tilt the stage. While this problem could have been solved with traditional, combined left/right motion control using software like LabVIEW[4], we used an innovative approach using multi-touch finger gestures on a tablet PC. Finger input provides a more natural input than using the mouse pointer. Furthermore, a tablet PC provides mobility of the user who is no longer restricted to operate the software on rack-mounted computer in a remote place. The software has been written in Python, the Graphical User Interface (GUI) is designed with Kivy[5]. Communication with the Picomotor controller is realized via Ethernet.

---

[3] Picomotor™ is a trademark of NEW FOCUS, Inc.

[4] LabVIEW™ is a trademark of National Instruments Corporation.

[5] http://www.kivy.org

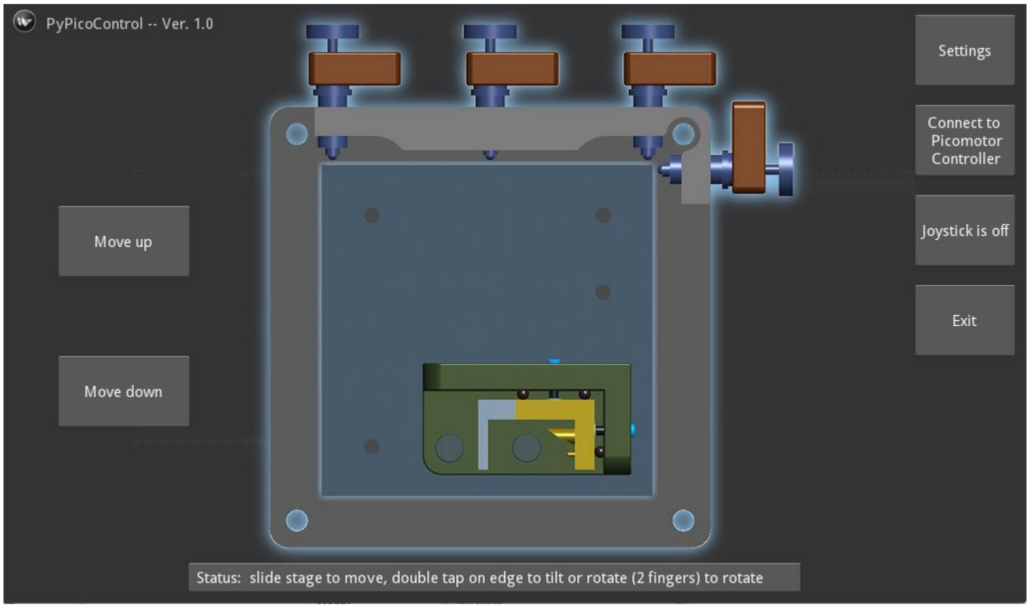

Status: slide stage to move, double tap on edge to tilt or rotate (2 fingers) to rotate

Figure 11: Motion control interface for the EPM goniometer.

Figure 11 shows a screenshot of the GUI. The GUI displays an interactive image (top view) of the stage. The settings button provides access to set the network IP address and port of the Picomotor controller, as well as the speed settings of the motors.

By sliding the stage with one finger in the desired direction the user can initiate translation motion. Putting two fingers on the stage and rotating one finger clockwise or counter-clockwise performs rotation of the stage. Double pressing and holding a finger at the corner or edge that the user wants to “push down” initiates tipping or tilting of the stage. Separate buttons next to the stage control up/down motion of the whole stage.

Figure 12 shows some examples of stage movements. The fuzzy, cyan-colored blob represents the finger. The red pictogram is an animated motion indicator, which appears when the stage starts moving. The status bar on the bottom also indicates the current movement. As soon as the finger is lifted off the screen the motion stops.

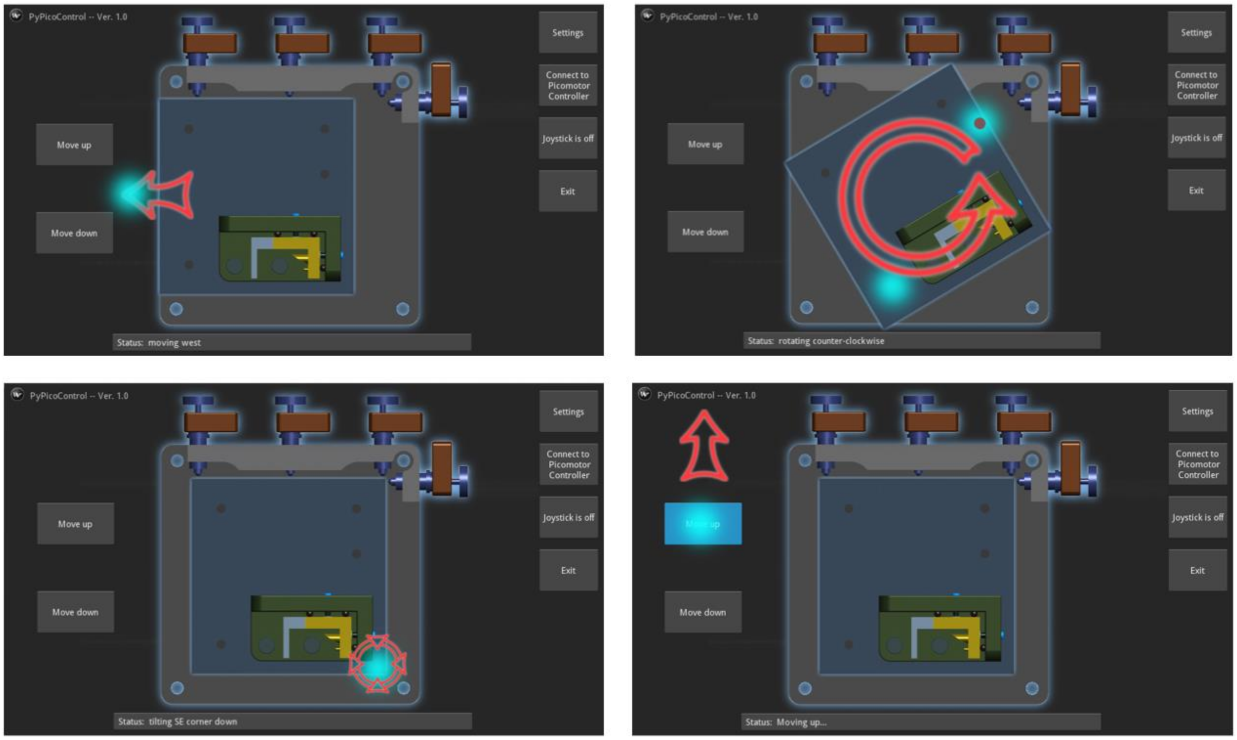

Status: moving west

Status: rotating counter-clockwise

Status: tilting SE corner down

Status: Moving up...

**Figure 12: Examples of different stage movements.**

### *2.1.3. Focusing Tests*

We acquired two alignment prototypes from MPCL in FY 2012. We had planned to acquire more EPMs in FY13. Unfortunately Sandia decided to shut down support for MPCL, which brought this part of the project to a premature end.

However, focusing tests were performed with the alignment prototypes. A continuous-wave HeNe laser (λ = 623 nm) was expanded to 2″ diameter. An $f/\# = 4$ lens simulated the OAP used in the 100 TW target chamber. Figure 13 shows a birds-eye view of the experiment. The beam expander of the HeNe can be seen on the right side. Coming from the right, there is a filter holder to attenuate the laser with neutral density (ND) filters. Close to the EPM goniometer is the focusing lens. The LEH of the EPM is placed at the lens focus. The EPM re-directs the beam upwards. An about 30× magnification, long-distance microscope images the EPM focus onto a camera. In the top left corner is the tablet PC with the motion control GUI. Underneath the lens one can see another objective, rotated by about 45°. This camera was used to image the LEH area and to align the LEH for maximum transmission.

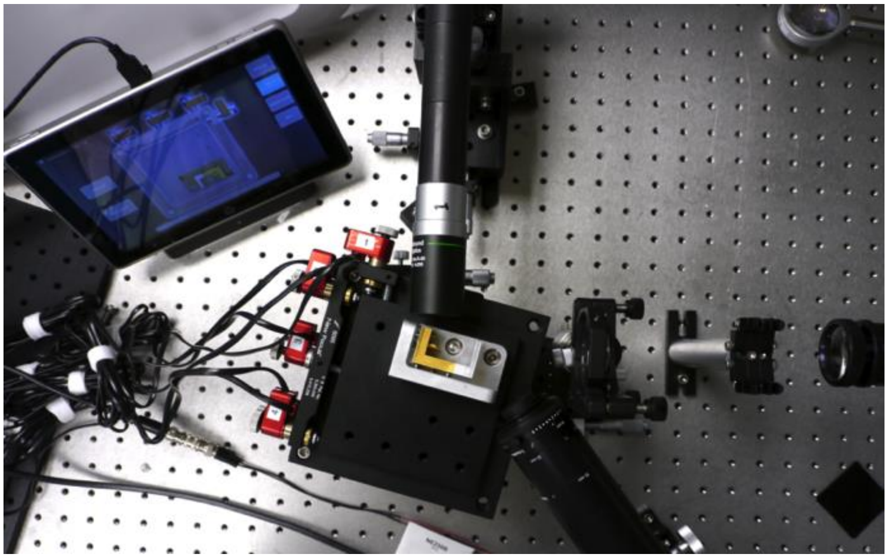

**Figure 13: EPM focusing test with a cw HeNe laser.**

Figure 14 shows the test focusing results. The left image shows the HeNe laser focus in front of the EPM. Is has a 5.4 µm FWHM, which is almost exactly as large as the ZPW focus in the 100 TW target chamber. The right side shows the focus behind the EPM. The beam has been demagnified to 1.6 µm FWHM, which corresponds to a demagnification of 3.3. Although this is not the designed 4× demagnification, it is very close. The difference is attributed to imperfections of the EPM surface from the diamond turning. Note that a 3.3× demagnification results in an ≈11× intensity increase!

Beam pointing improvement tests, as well as reflectivity tests using the pulsed, unamplified ZPW beam are still pending.

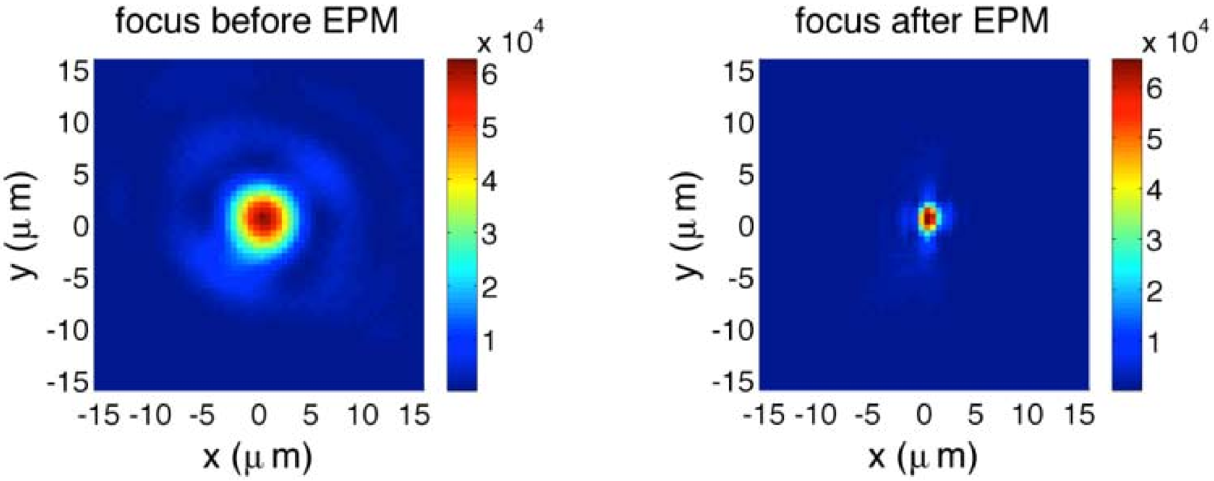

**Figure 14: EPM focusing tests.** *The left image shows the HeNe laser focus in front of the EPM. Is has a 5.4 µm FWHM, which is almost exactly as large as the ZPW focus in the 100 TW target chamber. The right side shows the focus behind the EPM. The beam has been demagnified to 1.6 µm FWHM.*

## 2.2. PROTON DETECTOR FOR Z

Proton detection at Z needs most likely to be done very close to the center, since the divergent proton beam quickly loses signal strength. Org. 01672 started to develop the Compact Point-Projection System (C-Pops) in CYs 09-11. This detector was designed to be a small, close-distance prototype for the image plate housing for ZPW-driven, high-energy x-ray backlighting. Figure 15 shows C-Pops in a ride-along experiment at Z shot z2172, which was part of the Lincoln shot series in CY 2011. The detector is made out of Tungsten for maximum x-ray background and debris protection. The Z load-facing side has a ≈5×5 mm$^2$, square opening, which frames the field of view. Filters were 75 µm of indium, 2 mm of Kapton[6] and 2 mm of aluminum. The Kapton and aluminum were distributed over eight 250 µm thick sheets and split into 4 sheets each for a front aperture filter and a secondary filter in contact with the IP.

Due to the similarity of the application, C-Pops can be used to detect protons as well as x-rays. While the rather small entrance aperture would not permit to detect a magnified proton radiographic image, it is large enough to detect the deflection of a pencil beam due to EM-fields.

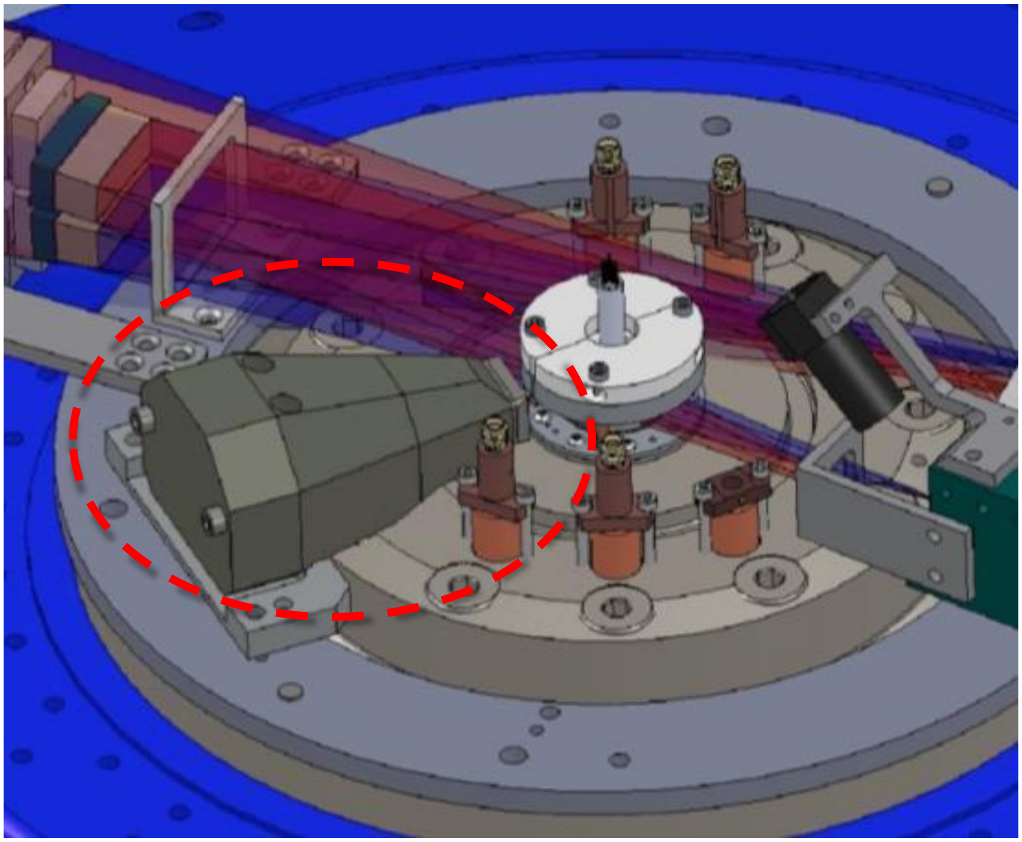

**Figure 15: C-Pops (encircled by the red, dashed ellipse) in a ride-along shot at Z.** *Image courtesy of Grafton Robertson (SNL).*

---

[6] Kapton® polyimide film is a registered trademark of E.I. du Pont de Nemours and Company or its affiliates.

RCFs were placed inside C-Pops for a background test during a ride-along at Z shot z2171. This experiment imploded a cylindrical Be liner to measure Magneto-Rayleigh-Taylor instabilies with 6.151 keV, bent-crystal x-ray backlighting. These results have been published in Ref. [46]. C-Pops was configured as shown in Figure 15. The distance of the RCF detector inside C-Pops the center of the load was 10.2 cm. One HD-810 RCF and one MD-V2-55 RCF were placed inside C-Pops to measure the x-ray background. Protons with energies above 25 MeV are able to penetrate the filters.

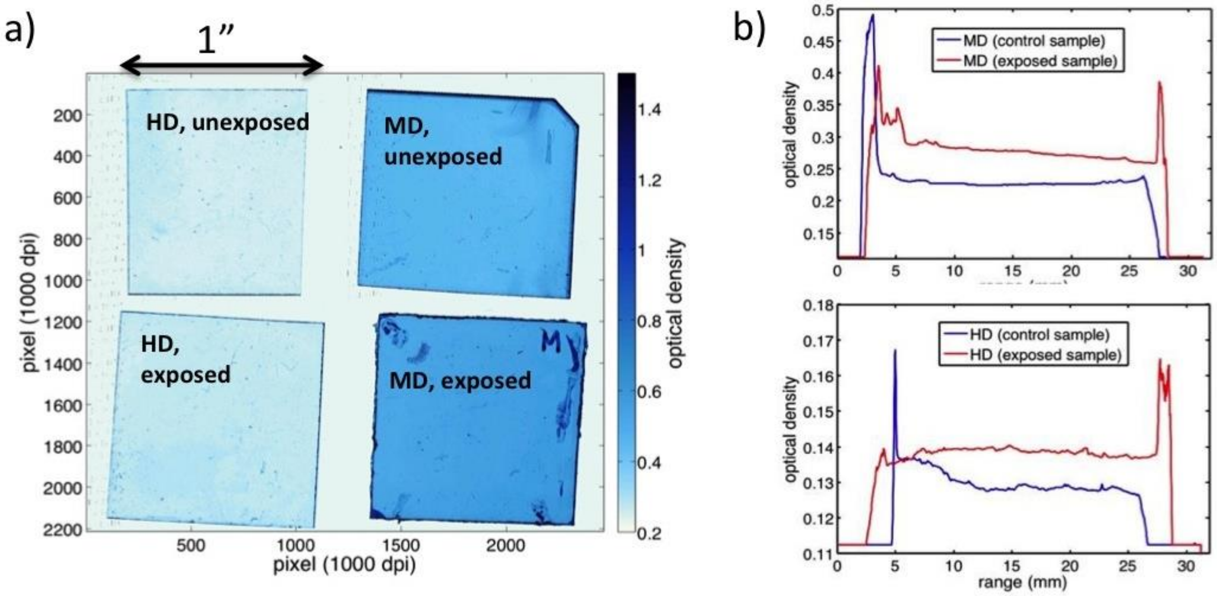

**Figure 16: Z background measurement with RCF and C-Pops.**

Figure 16a shows the exposed films after the shot, compared to control samples from the same RCF batch that were not irradiated. Figure 16b shows the corresponding lineouts, averaged in vertical direction. While there is some additional signal after the shot, it is very small and uniform.

These results are encouraging and suggest that RCF within C-Pops can indeed be used to detect protons near Z's center. Note that if a future experiment encounters significantly increased x-ray background and/or very low proton signals, one could use CR-39 solid state nuclear track detectors. CR-39 is not sensitive to either electrons or x-rays and has been widely used as a high energy ion diagnostic [4,8,47]. CR-39 can detect single proton tracks. However, data analysis is much more time-consuming than for RCF since CR-39 need to be etched up to several hours in NaOH solution to reveal the particle tracks. After that, the individual tracks need to be counted using a high-resolution microscope and specialized track recognition software, which takes up to 24 hours per CR-39.

# 3. ION BEAM REQUIREMENTS FOR RADIOGRAPHY OR DEFLECTROMETRY AT Z

This section presents some charged particle tracking results for an idealized, but representative liner implosion experiment at Z. The tracking was performed to determine if charged particle radiography would be feasible at Z, and which particle energies would be required. Different heavy ions as well as relativistic electrons were tracked to find out which particle species would be best suited.

## 3.1. CHARGED PARTICLE TRACKING

The trajectory of a charged particle in a (static) electromagnetic field is determined by the equation of motion

$$\frac{d\boldsymbol{x}}{dt} = \boldsymbol{v}, \tag{4}$$

and the Lorentz force

$$\frac{d\boldsymbol{p}}{dt} = \frac{Zq}{m}(\boldsymbol{E} + \boldsymbol{v} \times \boldsymbol{B}), \tag{5}$$

where $\boldsymbol{p}$ denotes the (relativistic) particle momentum vector, $Z$ its nuclear charge state, $q$ the elementary charge, $m$ the particle mass, $\boldsymbol{v}$ the particle velocity vector, $\boldsymbol{E}$ the electric field and $\boldsymbol{B}$ the magnetic field vectors of the laser wave, respectively.

The next section presents a model scenario for the EM-field distribution at Z. The fields are either known analytically or as a two-dimensional slice through the cylindrical geometry. Instead of converting those fields to a suitable, 3D array for a tracking code (LSP, GPT, GEANT, etc.), and spending some time learning how to use the tracking code, it was decided to write a particle tracer in MATLAB[7] since the problem of tracking one or a few particles through the fields is simple enough and well documented. The numerical solution of equations (4) and (5) was performed with a standard Leapfrog method to advance the particle position over time. The particle push by the Lorentz force was performed using a relativistic Boris particle pusher [48].

## 3.2. CHARGED PARTICLE RADIOGRAPHY OF AN IMPLODING CYLINDER

An imploding cylinder, driven by the MA current of Z, will serve as the test scenario for charged particle radiography. The $B_\Theta$-field that drives the Z-pinch is the strongest part of the EM-fields at Z. It is similar in magnitude and shape for gas puff experiments, dynamic hohlraums, imploding wire arrays or Dynamic Material Properties (DMP) experiments using flyer plates. Hence, the particle tracking results for this scenario are representative for many experiments performed at Z.

---

[7] MATLAB® is a registered trademark of The MathWorks, Inc.

The setup is as follows: The imploding cylinder (liner) is driven by a 20 MA current, flowing from top to bottom. This current generates an azimuthal $B_\Theta$-field. The return current flows through the return-current can, $B_\Theta$ is confined to the space between liner and return-current can. The liner is assumed to have 1 mm radius, the return-current can has 13 mm radius. This system is a coaxial system with the liner's outer radius being the inner conductor and the return-current can's inner radius being the outer conductor. Thus the azimuthal $B_\Theta$-field can be calculated as

$$B_\Theta(r) = \frac{\mu_0 I}{2\pi r} = 20 \times \frac{I\,[MA]}{r\,[cm]}. \tag{6}$$

At the return-current can surface $B_\Theta$ is ≈ 300 T, and at the cylinder surface it rises to 4000 T. There is an electric field $E_z$ due to the voltage drop across the liner, this field is assumed to be uniform with $2 \times 10^8$ V/m, pointing in –z-direction. The liner is centered at (x,y,z) = (0,0,0). Both liner and return-current can have ±3 mm height, above or below that there is a field-free vacuum (other hardware in reality).

Figure 17 shows a schematic of the configuration. The green cylinders represent the liner and the return-current can, respectively. The blue arrows represent the azimuthal $B_\Theta$-field. The length of the arrows represents the field strength according to eq. (6).

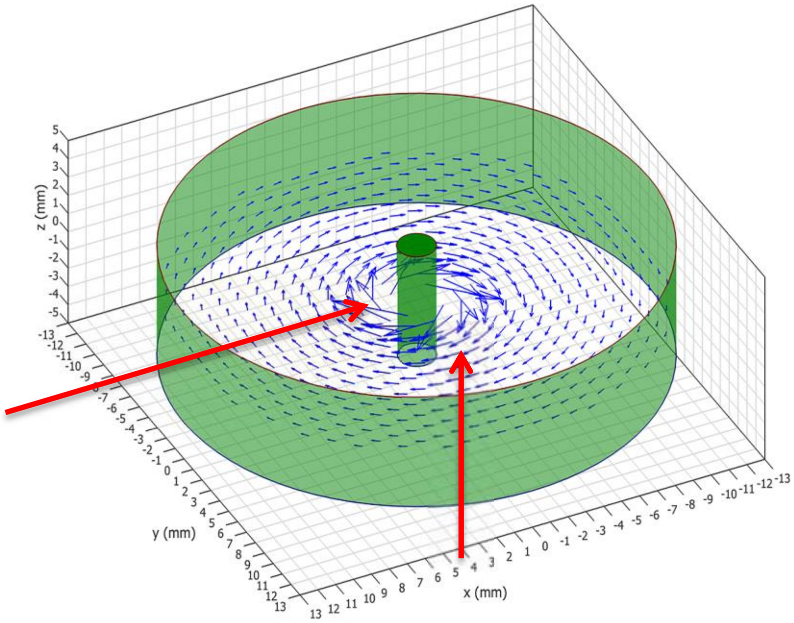

**Figure 17: $B_\Theta$-field of an imploding cylinder.** *The red arrows show the injection trajectories.*

Next, the tracking code was used to inject protons into this field, either in horizontal or in vertical direction. The protons have 40 MeV, which is the maximum energy to be expected using ZPW at Z (see sec. 1.3). The protons are either injected at (x,y,z) = (0,-13,0), and propagate in positive y-direction, or they are injected at (0,3,-5) and propagate in positive z-direction. Each beam consists of 50 protons, with random angular distribution between ±20°. These two scenarios are designed to probe the liner either perpendicularly or parallel to the z-axis.

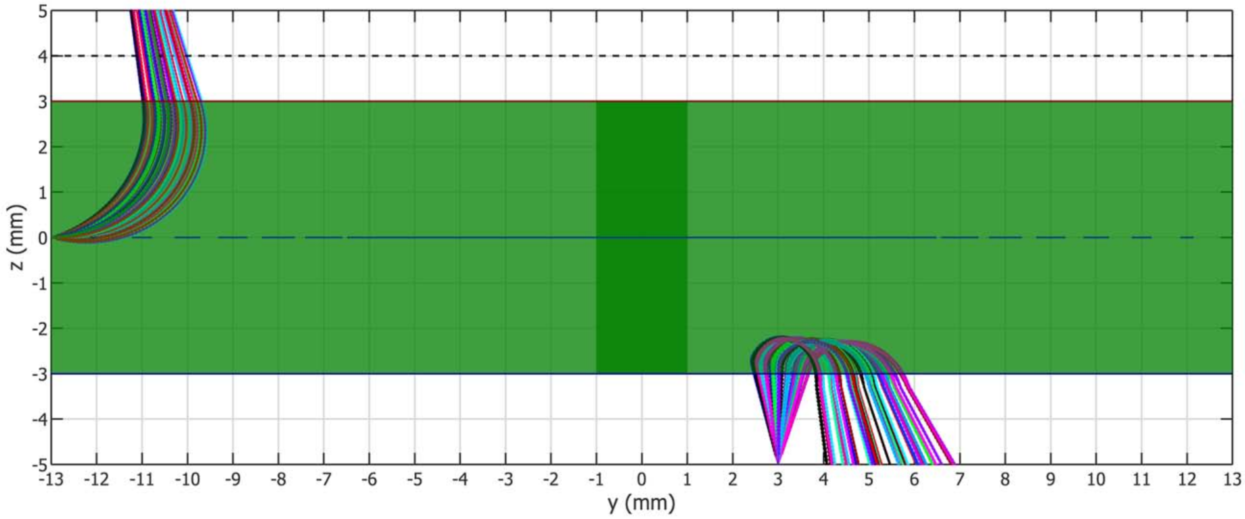

**Figure 18: 40 MeV proton tracking results in a 20 MA liner Z-pinch implosion.**

Figure 18 shows the tracking results, as seen from the side. The protons did not propagate very far before they got deflected by the $B_{\Theta}$-field, which forced them to turn around. They do not get even close to the liner. As soon as their z-position is above/below ±3 mm, there is no field and they propagate along a straight line. Thus performing *radiography* with laser-accelerated protons (or heavier ions) seems hopeless at the moment.

In order to do an actual radiography of the imploding liner, the protons would need about 4.5 GeV! Such energies are well beyond the present capability of laser acceleration. However, computer simulations suggest that future lasers might be able to reach those energies [49]. If 4.5 GeV protons, with ±15° angular spread are injected at (0,-13,-2.7) mm, they indeed generate an image/deflectogram of the field structure, as shown in Figure 19.

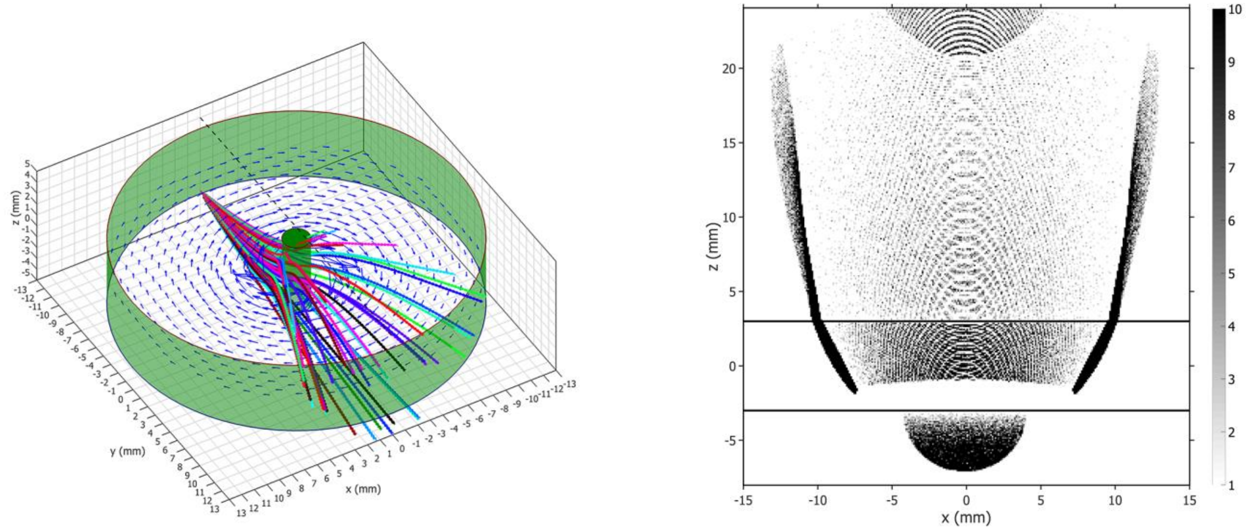

**Figure 19: Imploding liner radiography with 4.5 GeV protons.** *The left side shows a bird's eye view of 50 representative trajectories. The right side shows a detector image at y = 20 mm. The horizontal black lines represent the height of the liner and return-current can.*

## 3.3. CONCEPTUAL MAGNETIC FLUX COMPRESSION FRINGE FIELD MEASUREMENT AT Z

Liner radiography seems hopeless with current technology. However, ion *deflectometry* could be feasible. One scenario could be to measure the compressed magnetic flux of an axial seed field during cylindrical liner compression [40] by measuring the deflection of a laser-generated ion beam. A similar experiment has been done before using laser beams to compress the liner [39], although on much smaller spatial scales than at Z and not for the fringe field.

### 3.3.1. Model Scenario

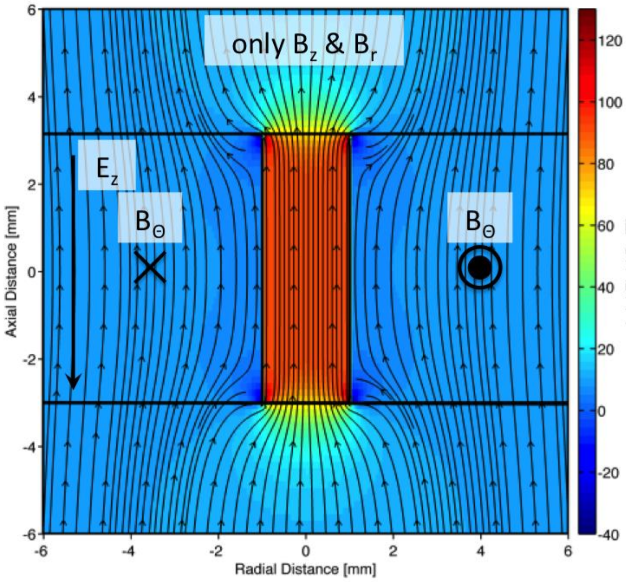

**Figure 20: Magnetic and electric fields for a flux-compressed, Bz = 10 T seed field.** *Data courtesy of Ryan D. McBride (SNL).*

Similar to the liner compression example from above, Z compresses a hollow cylinder with its $B_\Theta$-field. A 20 MA current is assumed. In case of a flux compression experiment an initial, uniform seed field is applied along the z-axis. Figure 20 shows the resulting $B_z$-field after the initial r = 3 mm liner has been compressed to r = 1 mm. Ryan McBride (Org. 01688) provided the calculations and data. The field solution has been generated by a simplified calculation of magnetic flux compression. Note that this field solution ignores the effects of the surrounding electrodes and other load hardware nearby. In this idealized example it is further assumed that the $B_\Theta$-field abruptly ends for $|z| > 3$ mm.

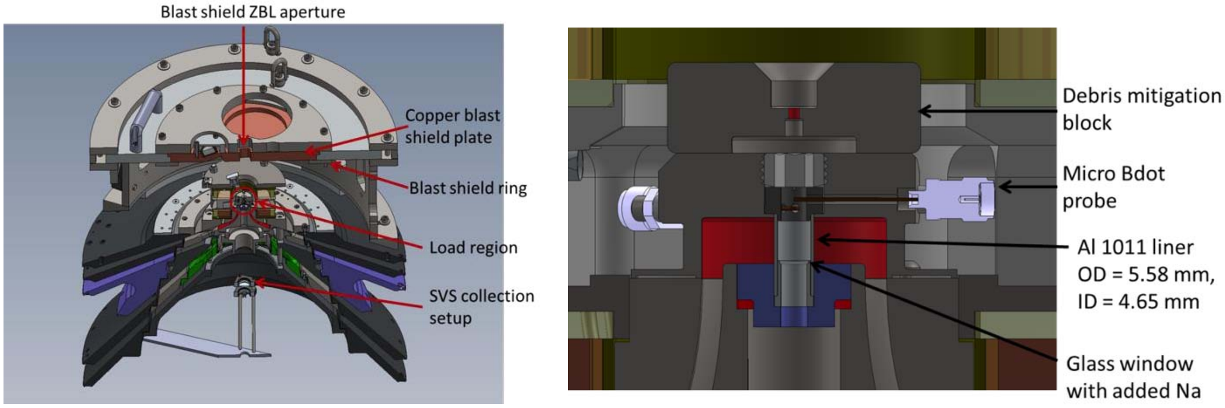

**Figure 21: CAD drawings of the Roosevelt 2 shot series.** *Images courtesy of Adam J. Harvey-Thompson and Ryan D. McBride (SNL).*

In reality there will be the magnetically-insulated transmission lines (MITL) on the bottom and other load hardware at the top, which will cause the field to decay (see Figure 21 for an example).

The initial 10 T seed field has been compressed to about 100 T. In the fringe field region on top of the liner (for z > 3 mm) there is still significant field modulation that could be detected. The simplified calculation neglects an azimuthal electric field, which occurs due to the changing $B_z$-field according to the Maxwell-Faraday equation $\nabla \times E = -dB/dt$. A crude estimate taking the compression time for implies that will be on the order of MV/m. Thus, a proton propagating through the ≈ 2 mm field would gain a few keV energy. This is certainly negligible compared to the tens of MeV energy the proton already has.

### 3.3.2. Tracking Results

Figure 22 shows particle tracking results, seen from the top. The particles were injected at (0,-13,4) mm, i.e., directly at the return-current can's inner radius and 1 mm above the liner. Without flux compression, charged particles will be deflected in the uniform, 10 T $B_z$-field. The deflection $\Delta x$ after some propagation can be calculated with the help of the Larmor radius $r_L = \gamma m v / ZqB$ as $\Delta x = r_L - (r_L^2 - d^2)^{1/2}$. The Larmor radius is plotted as the faint, red line in Figure 22.

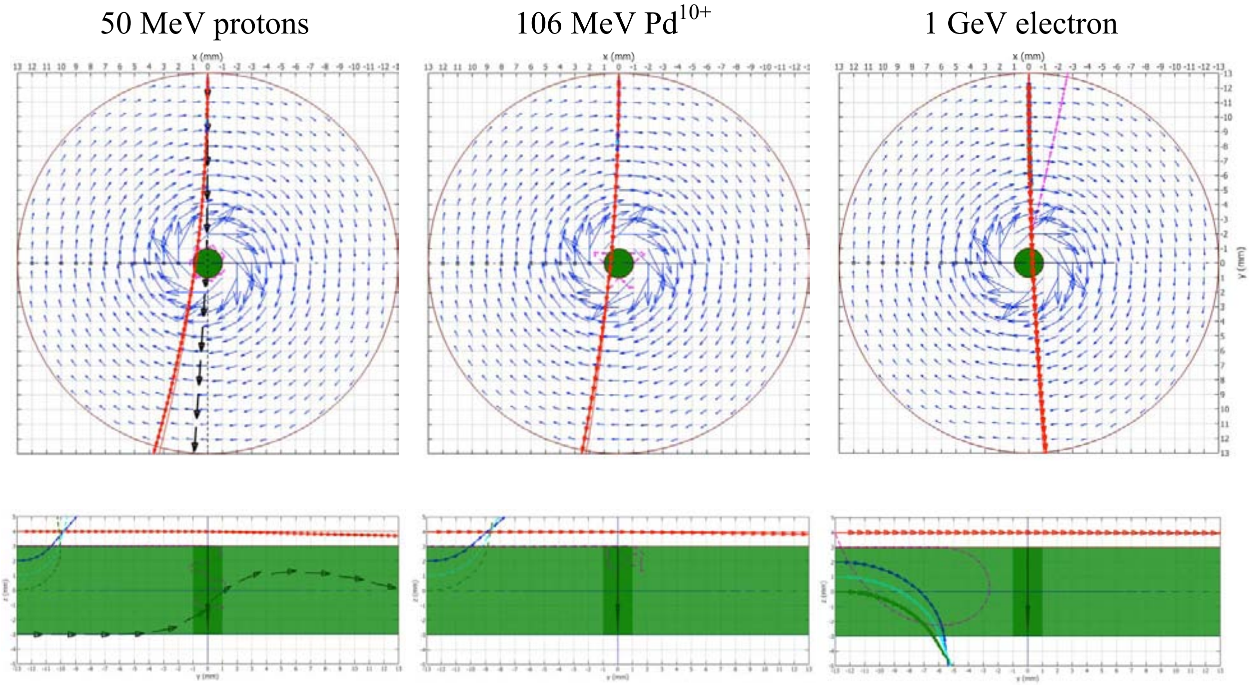

50 MeV protons

106 MeV $Pd^{10+}$

1 GeV electron

**Figure 22: Fringe field tracking results for protons, heavy ions and relativistic electrons.**

The left plot shows tracking results for 50 MeV protons (red line with small arrows). The other trajectories are for protons injected at z ≤ 3 mm. The black trajectory is for a 3 GeV proton injected at z = -3 mm, to demonstrate again that GeV energies are required to penetrate the liner.

Although the protons penetrate the liner area just barely, there is some additional deflection compared to the trajectory in the uniform field. At the exit of the return-current can, the static B-field deflection is $\Delta x = 3.3$ mm. With flux compression the deflection is $\Delta x = 3.7$ mm.

A very similar picture is created by using 106 MeV $Pd^{10+}$ [50] as an example for a laser-accelerated heavy ion. Heavy ions are magnetically stiffer due to their higher mass; however their charge state is also higher. In the example here, the Pd ions penetrate the liner slightly closer to the center than the protons; however the overall change of deflection is comparable to protons. A somewhat similar result was obtained using $C^{4+}$ [51] (not shown).

Shortpulse lasers are not only able to accelerate ions, they have been very successfully used to generate mono-energetic, GeV electrons with laser-wakefield acceleration (see the review article by E. Esarey *et al.* [52]). The right plots of Figure 22 show tracking results for a 1 GeV electron (red, the other trajectories are for injection at $z \leq 3$ mm). While a GeV electron is able to propagate to the center of the compressed liner, the trajectory with flux compression is indistinguishable from the trajectory in the seed field.

The results presented here show that protons are as good or as bad to measure the flux compressed fringe field as other particles. However, protons are the easiest to accelerate because untreated foil targets always result in proton beams when irradiated by an intense laser pulse. Efficient heavy ion acceleration requires to clean the target surface from the hydrocarbon impurities, which so far has only been efficiently achieved by heating the target to a high temperature [53,54]. GeV-scale electron acceleration requires a well-controlled gas jet and laser propagation in direction of the electron beam. A horizontal injection of a shortpulse laser into Z seems to be a challenging engineering task. Furthermore, ZPW's pulse is too long for plasma wakefield acceleration; the laser hardware would need to be significantly modified to permit shorter pulse durations than the current ≈ 500 fs.

### *3.3.3 A Working Case*

The previous section has shown that protons might be applied to measure the flux compressed fringe field. The source needs to be shifted in –x-direction, such that the deflection in the seed field causes the protons to penetrate the center of the liner. The proton energy should be as low as possible to gain maximum additional deflection in the compressed field region. Protons with low energy will also increase the signal strength due to the exponential proton spectrum.

Figure 23 shows a potential working case. The source was offset to $x = -1.1$ mm, $z = 4.5$ mm. An 8 mm long collimator or aperture restricts the divergence of the beam to ±2.5° and creates a pencil beam. About $10^9$ protons with 30 MeV energy (see Figure 2) will be within this pencil beam. A square mesh with 10 µm wire thickness and 50 µm period was placed at the aperture position. The beam is cut for $z < 3$ mm, since this is the $B_\Theta$-field region and in a realistic scenario the protons would collide with some hardware and be stopped.

The top plot shows trajectories of the center and envelope, the bottom plot shown the beam profiles. The blue trajectories are without any field, the red trajectories are within the uniform, 10 T seed field, and the black trajectories are for the flux compression case. There is not only a shift of the centroid observable when flux compression is switched on, but also the mesh imprint is significantly deformed. Thus, there are two indicators for flux compression, both of which can be used to determine magnitude and shape of the flux-compressed $B_Z$-field.

The estimated signal strength at the detector at y = 20 mm is $\approx 10^8$ protons/mm$^2$. RCF would develop an optical density (OD) of 0.6 for HD-810 and OD = 1 for MD-V2-55. A CR-39 detector would be close to saturation, hence allow for a larger distance of the detector to the liner.

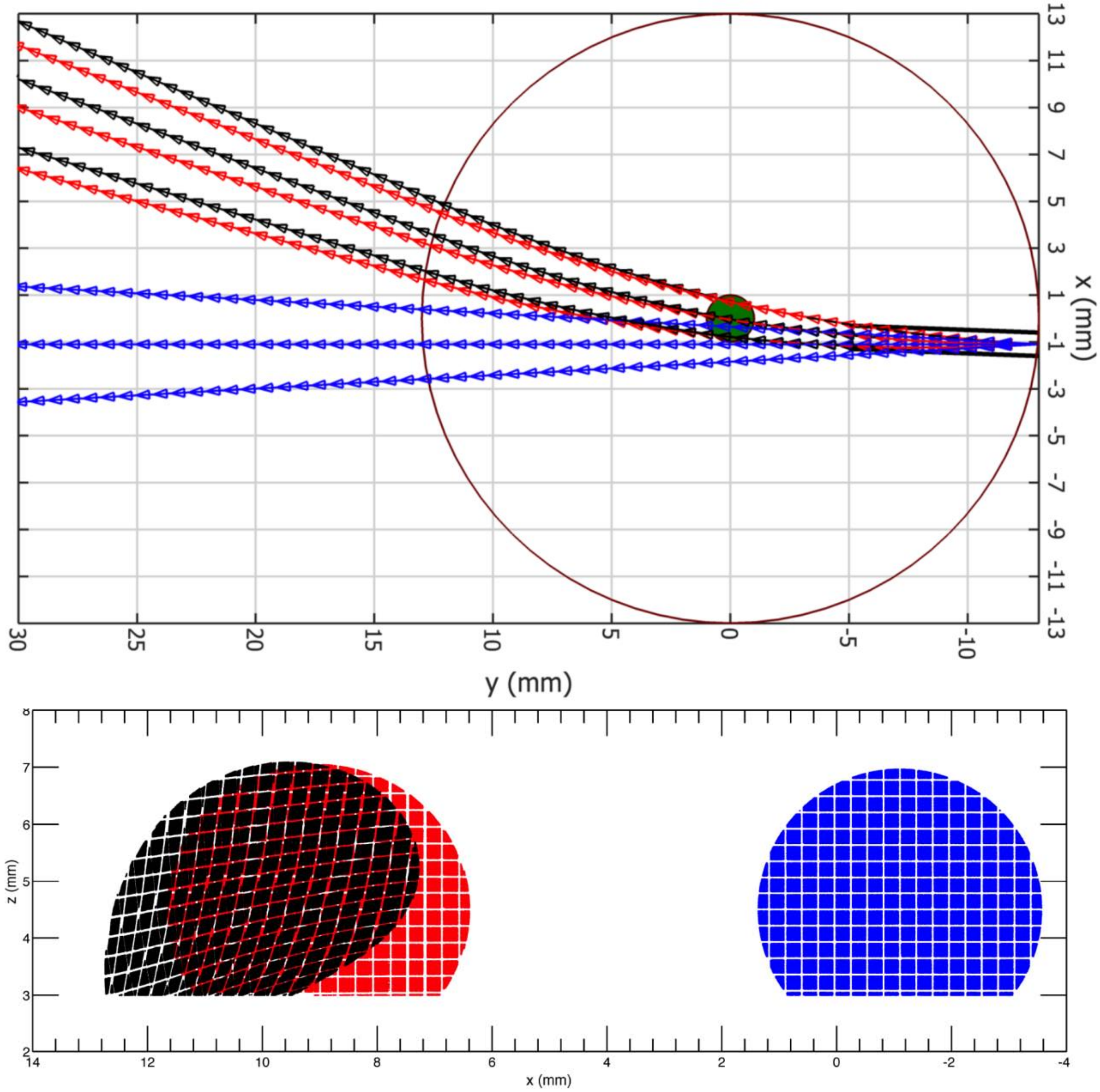

**Figure 23: 30 MeV proton tracking results to measure magnetic flux compression.**

This page intentionally left blank.

# 4. PROTON SOURCE MEASUREMENTS

## 4.1. MOTIVATION

The previous sections have shown that proton deflectometry might be feasible with ZPW at Z. The expected maximum energy using the long f-number FOA would be on the order of 30-40 MeV. This is close to the threshold energy required to penetrate the C-Pops filters. Furthermore, signal levels are relatively low near the maximum energy due to the exponentially decaying proton spectrum. Additionally, the maximum energy protons have a low divergence, which will cause a deflectometry experiment to be susceptible to pointing instabilities of the proton beam. A better method would be to use an aperture in some distance to the source to define the beam pointing.

Those concerns warrant an investigation of the proton source to optimize it for higher yield and higher energy. Proton beam parameters such as emittance, opening angle, spatial beam profile, energy spectrum, and maximum energy cutoff are sensitive to the electron energy distribution function (EEDF) [55,56], electron transport properties [57-59], direction of the incoming laser wave and its phase front [60,61] as well as target geometry [20,62,63] or size [64-69]. We have focused on the target geometry and laser incidence angle, as it can be easily changed without any changes to the laser infrastructure. Particularly, we scanned the target thickness over 2 orders of magnitude. The target transverse dimensions were either mm-size (large area foil, LF), or 250 μm (mass-limited target, MLT). The laser incidence angles were varied between 0° incidence, 45° *s*- or 45° *p*-polarization.

## 4.2. EXPERIMENTS WITH THE Z-PETAWATT AND TRIDENT SHORTPULSE LASERS

Experiments were performed with two HEDP laser systems: Z-Petawatt (ZPW) at Sandia National Laboratories (USA) and Trident at Los Alamos National Laboratory (USA). Both lasers have comparable irradiance $I = 2 \times 10^{20}$ W/cm$^2$, energy $E \approx 100$ J, and focal spot size of 6 μm FWHM. The main difference of the laser systems is their different temporal contrast. ZPW has a ns prepulse, whereas Trident is a high contrast laser system without ns prepulse. More details about the laser contrast will be discussed below.

The experiments at ZPW were conducted using the 100TW sub-system [70]. This Nd:glass laser system with OPCPA front-end delivers 100 J laser energy, in a sub-ps pulse with 1.054 μm wavelength. The laser is focused by an f/4, 8-inch diameter off-axis parabola (OAP) onto the target. The focal spot size is 5.7 μm FWHM, the first Airy minimum has 13 μm diameter. 27 % of the laser energy is contained in the FWHM, yielding a peak irradiance of $2\times10^{20}$ W/cm$^2$. The laser irradiated the target under 45°, by rotating the target either *s*- or *p*-polarization could be chosen.

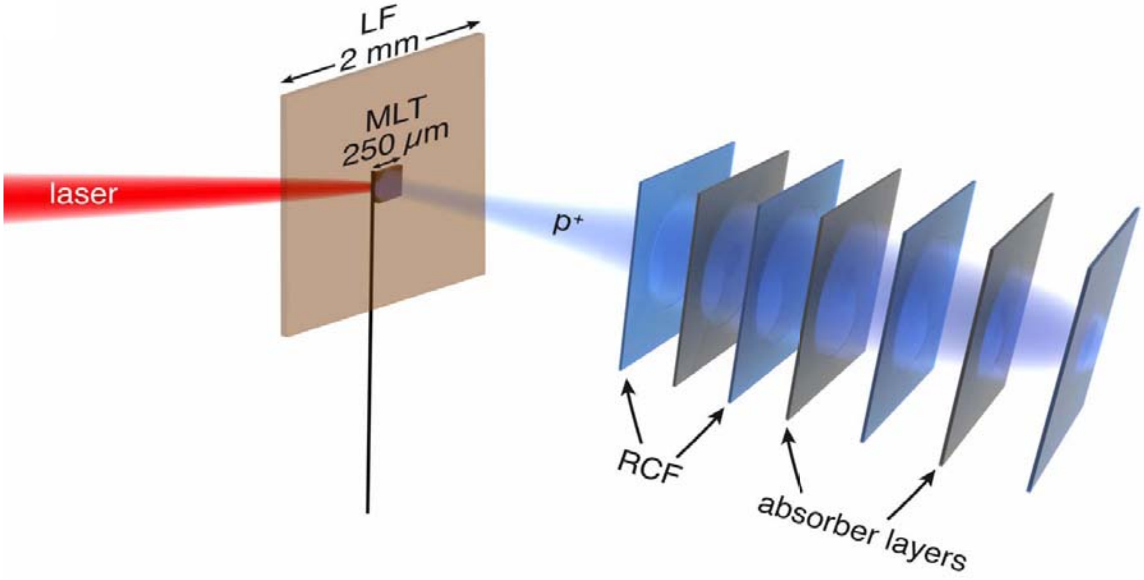

**Figure 24: Cartoon of the experimental set-up.** *The shortpulse laser is focused onto thin, Cu foils with either mm-long sides (Large Area Foils, LF) or onto mass-limited targets (MLT) with 250 μm sides. The protons accelerated from the rear side are diagnosed with a stack of radiochromic film (RCF). The RCF stack is interleaved with absorber layers to extend the energy measurement range while keeping the RCF count reasonable.*

The experiments at Los Alamos National Laboratory's Trident laser were performed with 80 J, in a sub-ps pulse with 1.054 μm wavelength. The laser is focused with an 8-inch, f/3 OAP to a FWHM of 6 μm [71], which contains 50 % of the energy. The peak irradiance is $2 \times 10^{20}$ W/cm$^2$. This laser irradiated the target under either normal incidence or 45° *p*- polarized.

The targets were commercially available Cu foils of with thicknesses between 1 and 125 μm, which were cut to either 2 × 1 mm strips (ZPW) or 2 × 2 mm square (Trident), free-standing targets, which are call large foils (LF). We have also prepared mass-limited targets (MLT, which have a radius less than the distance a hot electron can travel during the main pulse FWHM). Motivated by proton source size measurements at VULCAN PW [18], the MLT were either round or square disks with 250 μm diameter or side length. The MLT were glued with cyanoacrylate (CA) onto 7 μm thick, > 5 mm long carbon fibers at the end of a 1 cm long, 3 mm diameter Lexan stalk.

Stacks of calibrated radiochromic films were used to diagnose the proton beams. The stacks were placed 25 mm behind the target in target normal direction at ZPW. At Trident, the RCF-to-target distance was 38mm. At ZPW, the RCF stacks consisted of 8 layers of Gafchromic HD-810 film, followed by 14 layers of MD-V2-55. Apart from the first three layers, between each RCF layer was a layer of Ni absorber foils. The Ni layer thickness between each RCF pair was chosen such that the proton energy gaps between each RCF were about the same (3MeV) throughout the stack. The maximum detectable energy was 70 MeV. At Trident, we used Al instead of Ni. The energy gaps were between 2.5 and 3 MeV. 14 layers of MD-V2-55 followed 9 layers of HD-810; the upper detection limit of the stack was 85MeV. To protect the stacks from visible, UV and laser light, they were wrapped in 16.3 (25) µm Al foil at ZPW (Trident). On top of that was a layer of 50 (70) µm Kapton for debris protection.

The exposed RCF were scanned with a calibrated, white-light Microtek ArtixScan 1800f flatbed scanner at Sandia, and with a calibrated, white-light PDS/Perkin-Elmer 1010M micro-densitometer at LANL. Both scanner calibrations use the grey-scale mode, and agree within the 10 % error bar given by RCF batch-to-batch uncertainties [72]. Spectral and angular proton data unfolding was done with an improved method[8] to the one published in Ref. [18] to provide the three-dimensional (3D) particle number per (energy, {x,y} position) phase space, such as shown in Figure 25, which can be further reduced for a quantitative comparison to simulations.

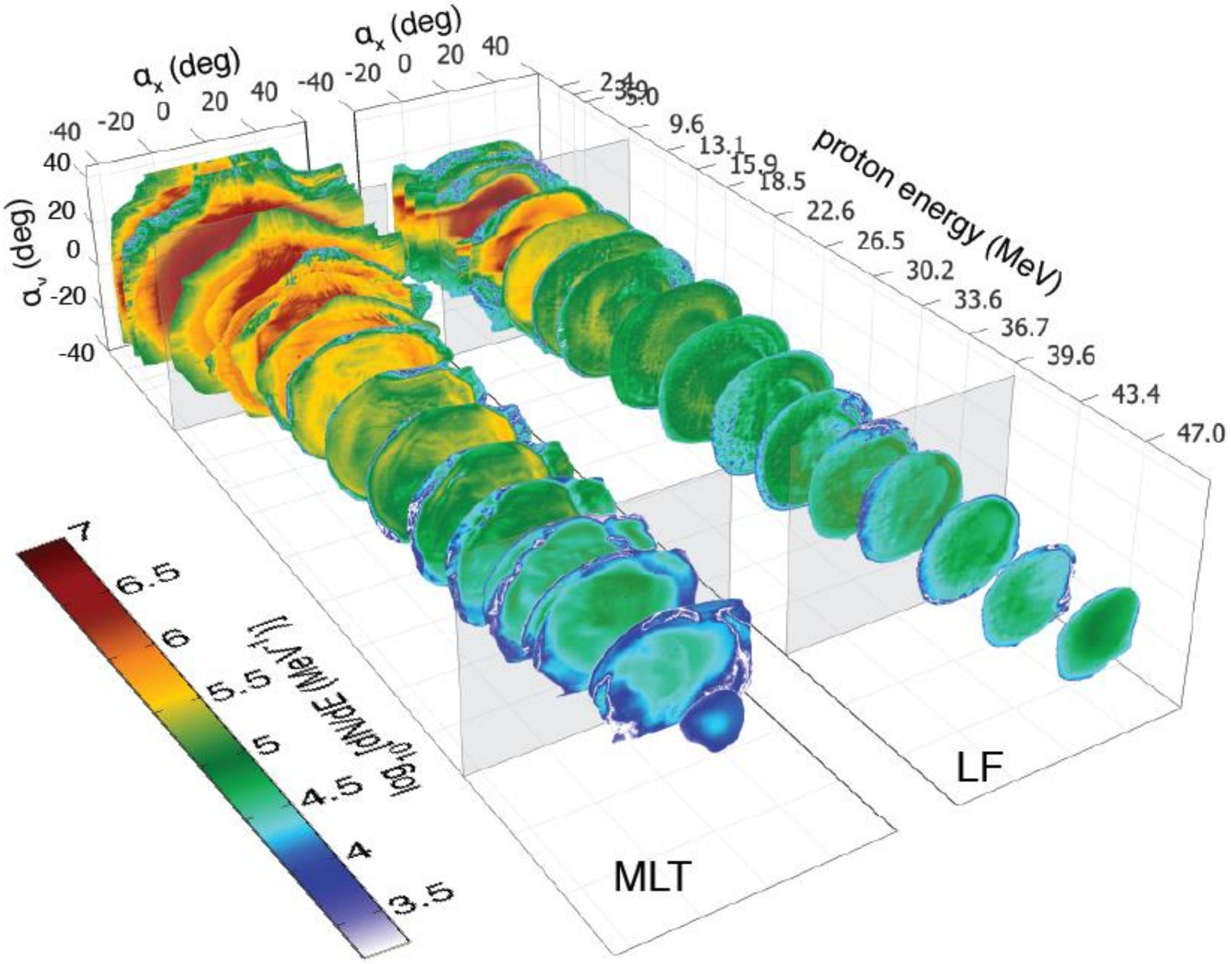

**Figure 25: Three-dimensional proton beam reconstruction in energy vs. position phase space.** *The left image is for MLT, the right image shows a LF result. Both targets yielded the same maximum proton energy, however the beam profiles are significantly different.*

---

[8] A publication of this method is planned to be submitted in October 2013.

## 4.3. LASER CONTRAST

The main difference between Trident and ZPW is the temporal contrast of the laser pulse. Specifically, ZPW has an about 1.5 ns prepulse [43], on which the main pulse sits, whereas Trident has seen tremendous contrast improvements over the last years [73] to eliminate the ns prepulse. To date, it is probably the best-contrast, high-energy shortpulse laser in the world.

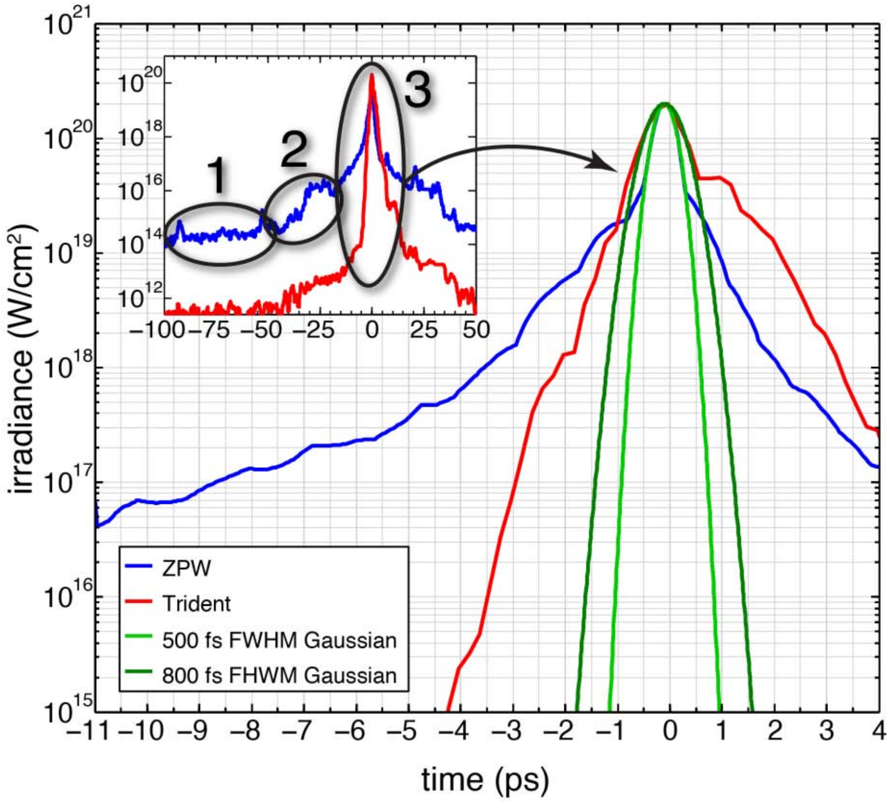

**Figure 26: Shot-averaged on-target irradiance vs. time**.*The blue line represents ZPW's irradiance, the red line represents Trident. Both laser pulses deviate from a Gaussian (green lines) for an irradiance below $10^{19}$ W/cm$^2$ and reach near-relativistic values (I > $10^{17}$ W/cm$^2$) several ps before the peak.*

Figure 26 shows the shot-averaged, on-target irradiance of the un-amplified (no rod and main amplifiers engaged) pulsed beams from both laser front-ends. The temporal pulse contrast at ZPW was measured with the third-order scanning cross-correlator SEQUOIA by Amplitude Technologies; at Trident the temporal pulse contrast was measured with the third-order cross-correlator Rincon 800 by Del Mar Photonics. Both measurements have been cleaned of known artifacts. Due to insufficient detector resolution ZPW's peak was replaced by a 500fs Gaussian between ±0.3ps, as measured by second order autocorrelation of the main pulse. Trident's data was kept unchanged.

The prepulse can be separated in three regions:

1. The ns prepulse pedestal,
2. A ps prepulse ramp, and
3. The main pulse.

As already mentioned, region 1 extends to -1.5 ns for ZPW [43]. Trident has no measurable prepulse for times earlier than -50 ps with respect to the peak [71]. A nanosecond prepulse creates a ns-duration blow-off preplasma and a shockwave propagates through the target. Simulations (see below) show that ZPW's prepulse creates a shockwave with velocity v ~ 8 μm/ns. As soon as the shockwave breaks out at the rear surface it creates a density gradient, which disrupts proton acceleration [74].

Region 2 is an intermediate region between the ns prepulse and the main pulse. Here, the intensity increases exponentially over several ps duration. ZPW's intensity is on the order of $10^{16}$ W/cm$^2$. In this intensity regime, hot electrons can be created as well as radiative preheat [75]. Trident's prepulse ramp is above $10^{12}$ W/cm$^2$; this intensity is well above the threshold to ignite a preplasma [76]. Our simulations (see below) predict that there is not preheat of the rear side for targets thicker than 12 μm at ZPW and 0.5 μm at Trident.

Region 3 is the main pulse. During the main pulse interaction with the plasma copious amounts of MeV electrons are created, which further heat the target, generate Kα-radiation and of course accelerate protons and heavy ions from the rear side. Note that both laser pulses deviate significantly from perfect Gaussian pulses (see the green lines). Both lasers have relativistic irradiance ( $I > 10^{18}$ W/cm$^2$) for more than 4 ps!

The ns prepulse (Region 1) is usually simulated using radiation-hydrodynamics codes. The transition region 2 requires more sophisticated codes; and depending on the code's capabilities either rad-hydrocodes are used or particle-in-cell (PIC) codes. The main interaction in region 3 needs to be simulated with PIC codes, since the interaction is far from any equilibrium and kinetic effects dominate.

## 4.4. EXPERIMENTAL RESULTS

Figure 27 presents a compilation of proton beam cutoff energy and laser-to-proton energy (> 5 MeV) conversion data from both lasers and LF vs. MLT target types, as well as the results from simulations. For lasers, LF show a similar thickness scaling down to 15 µm. Below 15 µm, the data from ZPW fall off due to rear-side shockwave breakout, which is confirmed by the simulations, whereas Trident's data continue to increase. The average energy for optimum target thickness is 50 MeV for both lasers; peak energies are 57 MeV for ZPW (15 µm thick LF) and 61 MeV for Trident (1 µm LF). Laser-to-proton energy conversion efficiencies are continuously increasing with thinner targets, and exceed 15% for Trident MLT. The high conversion efficiencies for the MLT coincide with a high particle count, derived by integrating the proton spectra (see Figure 2). LF targets produced about $10^{12}$ protons above 2.5 MeV whereas MLT generated about $10^{13}$ protons. Four features distinguish the MLT scaling (Figure 27b) from the LF scaling:

i. For most thicknesses, the average energies, peak energies, as well as energy conversion efficiencies are higher for MLT,
ii. The MLT maxima occur at a larger thickness than the respective LF maxima and they are different for both lasers,
iii. The MLT maximum energy and conversion efficiency are higher for Trident, and
iv. The MLT shot-to-shot fluctuations are larger near the thicknesses corresponding to the maxima (e.g. the 10 µm MLT from Trident vary between 75.4 MeV and 44MeV).

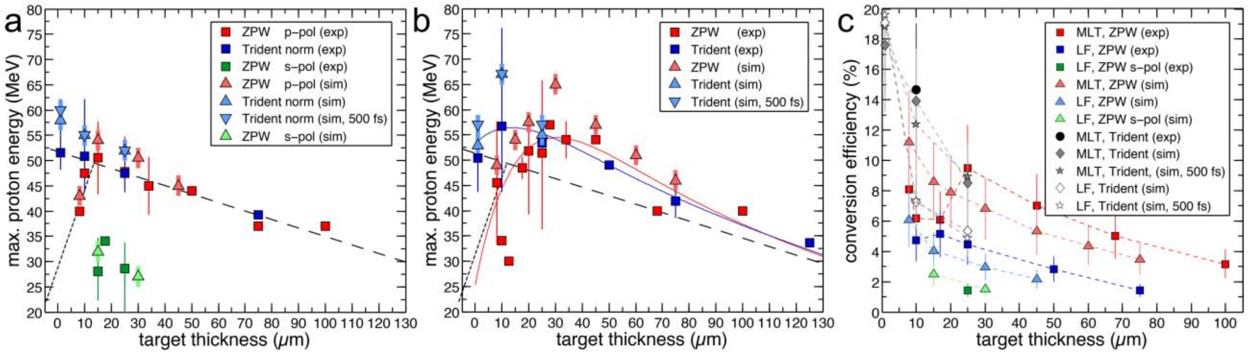

**Figure 27: Maximum proton energy and conversion efficiency vs. target.** *In **a** and **b**, the square and triangle symbols represent experimental data and simulation results, respectively, from ZPW (red) and Trident (blue) experiments using **a** large foil (LF) targets and **b** mass-limited targets targets (MLT). The data points are averages of all shots at a given thickness, and the error bars are the range from the minimum to maximum energies measured. The LF data for ZPW include s- versus p-polarization results. Error bars on the simulated maximum energies are estimated to be ±2 MeV. The dashed, dotted and red/blue lines serve as guides for the eye. **c** shows laser-to-proton energy conversion efficiencies for protons above 5 MeV. The square and diamond symbols represent experimental data and simulation results from ZPW, the circle and diamond symbols represent results from Trident. Note that at Trident both 1 µm target types result in the same max. energy.*

For all cases, the simulations quantitatively reproduce the measured data within shot-to-shot variations. Trident simulations have also been performed with 500 fs FWHM for $I > 2 \times 10^{19}$ W/cm$^2$ instead of 860 fs while keeping the integrated energy the same, to verify that a potentially shorter pulse [71] does not alter the observed scaling.

The higher proton energies and conversion efficiencies in MLT are explained by recirculation of the hot electrons within the smaller volume targets, leading to higher electron energy densities [64]. However, the reduction of proton energies for too-thin MLT suggests the existence of a proton density gradient prior to main pulse [77,78], which has been thought to be caused by ns prepulse heating [65,66] or preplasma wrap-around [63]. While ZPW has substantial ns-prepulse and thus preplasma extent, the 10 μm optimum MLT thickness at Trident cannot be explained by ns-prepulse heating or preplasma since the laser lacks ns-prepulse. However, the shift towards a thinner optimum MLT thickness and higher maximum energies for Trident compared to ZPW suggest that differences in the ps prepulse might explain the results.

Further differences between MLT and LF, depending on the laser system, are revealed by 2D slices of the proton beam profile. Figure 28a-e show 10 MeV energy slices for various target types. On ZPW, the beam profiles for MLT below optimum thickness exhibit fuzzy or filamented halo structures, which can reach up to 30 MeV. The beam-opening angle can be as large as ±40°. In contrast, all LF (Figure 28d) have round beams without halo and a lower divergence. At Trident, thin MLT (Figure 28e) do not show this fuzzy halo either. The presence of a fuzzy halo also affects the envelope divergence of the beams. Figure 28f compares various ZPW LF, which all exhibit the same slope, whereas g and h compare the divergences for MLT below and above optimum thickness, respectively. For too-thin MLT the divergence curves differ from LF, and regions with a knee exist. The Trident MLT data do not exhibit this knee. The curves for thicker ZPW MLT match the LF curves, however for normalized energies below 0.3 the divergence is much higher than the LF divergence.

While some parts of the data set can be explained by well-known ns preplasma effects (i.e., reduction of proton cutoff energy due to shockwave breakout at the rear surface, *s*- vs. *p*-polarization differences) or geometry effects (MLT yielding higher cutoff energies and conversion efficiencies), there is no simple explanation for the observed MLT optimum thickness for all cutoff energy and conversion efficiency, larger shot-to-shot fluctuations for MLT, the knees in the MLT divergence, and MLT fuzzy beam profiles.

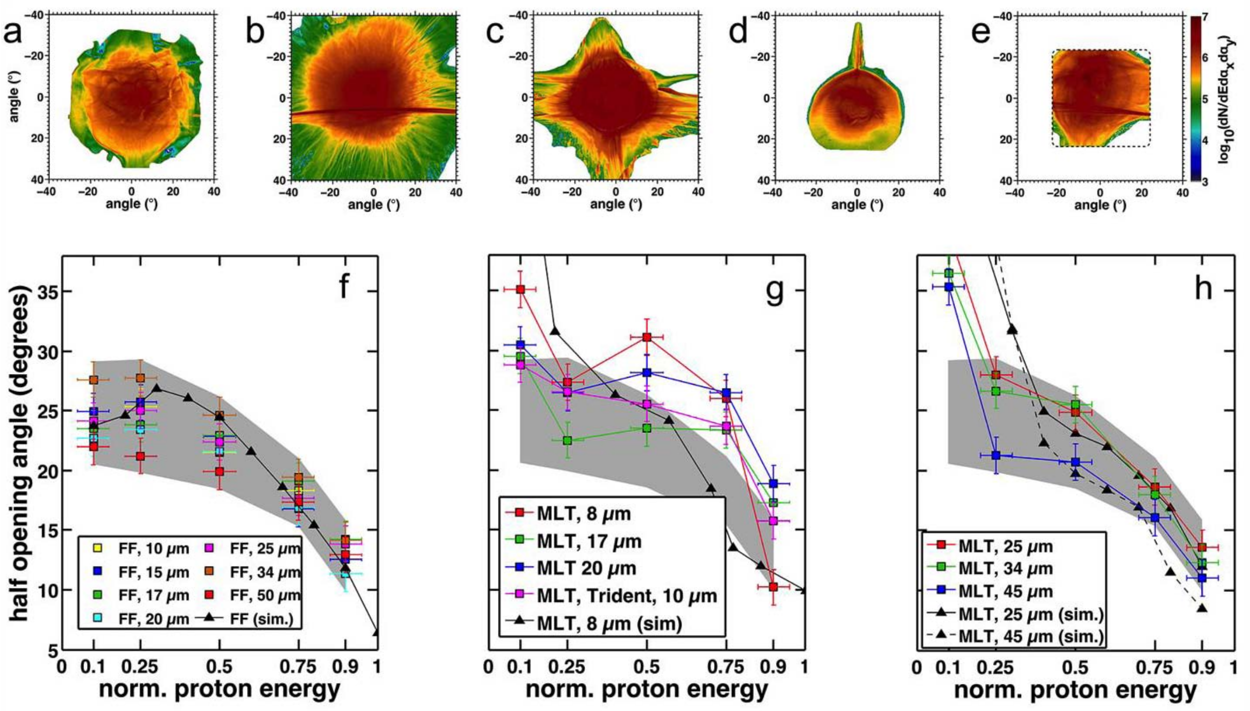

**Figure 28: Proton beam profiles and beam divergence.** ***a-c*** *beam profiles for ZPW MLTs with different thicknesses (10 µm, 25 µm and 45 µm),* ***d*** *profils for 10 µm thick LF, and* ***e*** *10 µm MLT at Trident, respectively. The dashed square in* ***e*** *represents the outside edge of the detector box. The half opening angle of the beam envelope (divergence) vs. normalized cutoff energy is plotted in* ***f-h****. Here, we normalized each shot to its respective cutoff energy for a better comparison.* ***f*** *compares different LF, which all have the same slope and fall within the grey area. For comparison, the same grey area is shown in* ***g*** *and* ***h****.* ***g*** *compares the divergence for thin MLT below the optimum thickness,* ***h*** *compares MLT above the optimum thickness. The data in* ***g*** *have knees in the slope and lie mostly outside the LF band. The data in* ***h*** *are within the LF band and show the same slope for norm. energies above 0.25. Lower energies have a much larger divergence, which is due to acceleration of the preplasma. Note that thin Trident MLTs (****g****, magenta) lie mostly within the LF band and show no knee.* ***f-h*** *also show ZPW simulation results (black and gray triangles). Apart from deviations for normalized energies below 0.25, the data are well reproduced within error bars.*

# 5. FULL-SCALE NUMERICAL SIMULATIONS

Explaining the experimental data with TNSA models or numerical simulations turned out to require a significant effort. Initially, a literature survey was performed. The few relevant papers [63-66] either contained contradicting results to our measurements, or only had very hand-waving, unsatisfying explanations.

Although there are many one-dimensional scaling laws for TNSA protons [22,24,79,80], none of which fit our LF data. Simulations using the 1D plasma expansion code by Patrick Mora [81] turned out to be of limited usability because too many initial assumptions had to be made. 2D, explicit PIC simulations with either LSP [82] or PSC [83] using Gaussian laser pulses with the measured FWHM in space and time could also not explain our results. Particularly, the thinnest targets always resulted in the highest proton energies, in contrast to the experimental data.

Finally, we decided to simulate the whole interaction, from ns prepulse to fs main pulse, as close to reality as computationally feasible. The simulation methodology was as follows: first, the ns prepulse interactions and preplasma expansions were simulated in 3D using the radiation-hydrodynamics code HYDRA [84]. For ZPW's prepulse, the simulations started at −1.5 ns, with a 0.5-ns rise from zero to $10^{14}$ W/cm$^2$, which were then maintained for 1 ns until the data shown in Figure 26 beginning at -100 ps. Trident's prepulse simulation was started at -50 ps.

The mm-size LFs were simulated assuming infinite extension. Full-scale simulations were performed with MLT. The simulations resolved a 10 nm water layer on the target surface and used a refined mesh to correctly treat ablation near the edges. The laser absorption was modeled with inverse Bremsstrahlung, turning point deposition, and ponderomotive force tensor corrections. We included two overlapping Gaussians, one with 4 μm radius and one with 10 μm radius, to simulate the poorly focused parts of the laser pulses and with intensity ratios that matched the measured values.

We ran HYDRA with both $H_2O$ and hydrocarbon contaminant layers and saw only little difference in the preplasma density and temperature profiles, justifying the use of water as impurity layer.

The final HYDRA electron and ion densities, temperatures, ionization states, and electron and ion velocities were then translated and used as initial conditions for the 2D, explicit particle-in-cell simulation code LSP [77,82]. This method provides an almost seamless transition from ns prepulse to sub-ps main pulse simulation. The explicit treatment in LSP generates the most realistic particle distribution functions without assumptions (aside from time step and cell size) about the field behavior or plasma response. It has no free numerical parameters, but requires very small time steps (our typical time step is 10 attoseconds for a simulation that runs over 15 ps) and many particles per cell to reduce high frequency true numerical noise. Contrarily, an implicit treatment would not need to resolve the highest frequencies (electron plasma frequency) and smallest spatial scales (speed of light times time step) but requires numerical high frequency damping to run a simulation stably, which allows for free numerical parameters that need to be benchmarked.

LSP was used in its fully explicit, kinetic, electromagnetic, and relativistic mode, and included collisions among all particles. A particle-pushing routine not susceptible to the numerical Debye length instability is used. The simulations had absorbing boundary conditions. The laser field was launched as a converging, Gaussian beam with a focal spot size of 6 μm FWHM, and linear polarization.

For the ZPW simulations, the laser irradiated the target under 45°, at either *s*- or *p*-polarization. For the Trident simulations the laser was normal incident. The temporal laser profile was taken from Figure 26. LSP was set up with a grid ranging from $= [-250, 220]$ μm where is the target axis of symmetry, and from $= [-150, 3$ μm where is the target rear surface. The target normal points in direction. The grid size was different for each run, especially Trident at 0° vs ZPW at 45°, since the laser wavelength (1 μm) had to be resolved well. We also did numerical sensitivity studies to make sure we got the same answer at higher resolution and higher particles per cell. A typical simulation grid was around $10^6$ nodes and $10^9$ particles, for 1-2x $10^6$ time steps.

The simulations started (ended) at -11.5 ps (+4.5 ps) for ZPW, and -4.5 ps (+4.5ps) for Trident. One simulation run took about one week on Sandia's TLCC and TLCC2 systems, using 1024 CPU cores per simulation.

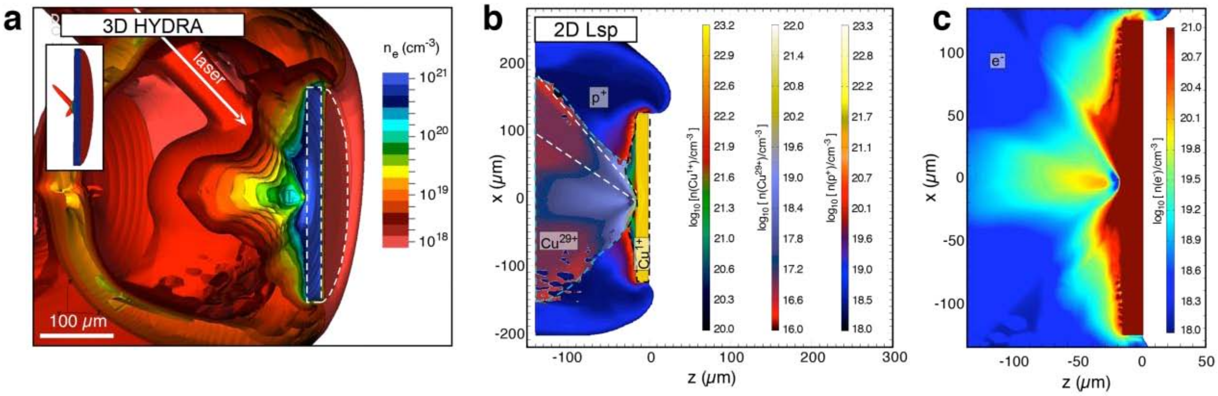

**Figure 29: 3D HYDRA simulation of ZPW's prepulse.** ***a*** *Electron density at the end of the ZPW prepulse for a 15 μm thick MLT. The inset shows the initial Cu half-disk for clarity.* ***b*** *Ion densities used for LSP initialization at -11.5 ps, shown as a 2D slice from the 3D HYDRA simulation in* ***a****. The white, dashed lines depict the incoming laser wave. The Cu ion charge states were reduced to $Cu^{+29}$ (encircled by the gray-blue, dashed line) in the expanding plume or $Cu^{+1}$ (black, dashed line) in and near the solid target, and protons replaced the $H_2O$. The laser prepulse creates a shockwave, which has propagated about 11 μm inside the 15 μm thick target (indicated by the light-yellow region within the target in* ***b****. However, the rear surface is still unperturbed, meaning that no significant expansion has taken place by the end of the prepulse.* ***c*** *shows a magnified view of the electron density. Plasma ablation and laser ponderomotive pressure modify the topology of the critical density surface ($n_e > 10^{21}$ cm$^{-3}$, dark-red), resulting in a strong gradient at the edge of the incoming laser.*

ZPW prepulse simulations are presented in Figure 29 for a 15 μm thick MLT. The water impurity surface layer (the source of protons) expands fastest and forms a shell (dark orange colored band) around the Cu material, which primarily consists of $Cu^{+29}$ in the expanding hot plume, a weakly-ionized region near the focal area, and a cold region in much of the bulk solid. The asymmetric laser incidence results in water preplasma wrapping asymmetrically around the target edges.

Figure 29b shows 2D density cuts of the three different ion species involved in the prepulse interaction: $Cu^{+29}$ in the hot preplasma, $Cu^{+1}$ for the weakly-ionized plasma and cold solid, and the water volume which has been reduced to only protons for the subsequent main pulse simulation. Ablation and laser ponderomotive pressure modify the topology of the critical density surface ($n_e = 1.1 \times 10^{21}$ cm$^{-3}$, represented by the blue region in Figure 29a or the green region in Figure 29b), resulting in a strong gradient at the edge of the incoming laser. A *p*-polarized laser (the electric field oscillates in the 2D plane and parallel to the gradient) skims a long interaction length prior to reaching the focal plane, leading to strong absorption and Brunel [85] or $\vec{v} \times \vec{B}$ electron heating [86] .

By contrast, *s*-polarization results in a reduction in electron heating and explains the *s*- vs. *p*-polarization differences at ZPW (Figure 27a) as a direct consequence of the preplasma structure. Due to the 45° incidence angle, this argument still holds in 3D, where the laser drills a tunnel in the preplasma [87]. The wrap-around preplasma contains protons of density $n_p \approx 10^{19}$ cm$^{-3}$. Thus, inclusion of the impurity layer in prepulse simulations is essential since this ion source can be accelerated forward and detected. Note that the simulations do not show a significant gradient at the rear surface.
The preplasma size for Trident is much smaller; simulation and interferometry data suggest it to be about 30 μm of half-spherical expansion. The prepulse-generated shockwave up to -4.5 ps is too weak to disturb even a 1 μm thin target.

Using only the measured laser and target parameters, the combined HYDRA and LSP simulations quantitatively reproduce all aspects of the available experimental data within error bars. These simulation results have shown this in the Figures in Section 4.4. The fact that the simulation results are on the high side of the error bars (shot-to-shot variability) in Figure 27 is attributed to the reduced dimensionality of the PIC modeling. Although general behavior and trends are similar in 2D and 3D [88,89], detailed comparisons revealed that 2D runs can result in slightly different particle energy densities because fields and densities do not spatially vary in the third dimension (y, here). This may result in small differences in expansion cooling (greater in 3D), pinching due to fields (greater in 2D), and geometric compression (greater in 3D). We estimate dimensionality to be an approximate 10% effect; however an explicit comparison for our work to an equivalent 3D case is not possible with present computational resources.

Another example for the outstanding agreement between simulation and experiment is the comparison of the $v_x$ vs. z phase space, which presents the distribution of transverse proton velocity $v_x$ vs. longitudinal position z. As can be seen in Figure 30a and b, the simulated beam profile matches the measured one not only in shape but also in absolute particle density. The black, dashed lines in the experimental data mark the upper angular acceptance of the RCF stack. In contrast to the LF data, the MLT has a “wing” next to the main beam. This wing is accelerated preplasma, which partly wrapped around the target edges. The preplasma overlaps with the main beam. It is indistinguishable from the main beam in the RCF detector. This additional $v_x$-

component explains the knee in the divergence data. The divergence angle Θ is proportional to $v_x/v_z$. The kinetic energy is proportional to $v_z^2 \sim z^2$. Thus a sudden increase of $v_x$ at a given position z results in a strong increase of Θ.

Figure 30c shows the simulation result for a 10 μm MLT at Trident. The beam profile is smooth and without wings. The yellow area is larger than the 30 μm ZPW data, which means the particle distribution is denser than at ZPW. Figure 30d shows the simulation result for an 8 μm thick MLT for ZPW. This target is thinner than the ≈11 μm distance the preplasma-generated shockwave propagates during the 1.5 ns long prepulse. It has already broken out at the rear side at the time when the main peak arrives. Shockwave breakout generates a density gradient, which weakens the accelerating electric field. Hence, the energy of the "main" beam protons is lower than the protons in the wings, which results in the wings overtaking the central beam in the figure. The large $v_x$ for nearly all z positions also explains the large divergence measured in Figure 28g for the thinnest MLT.

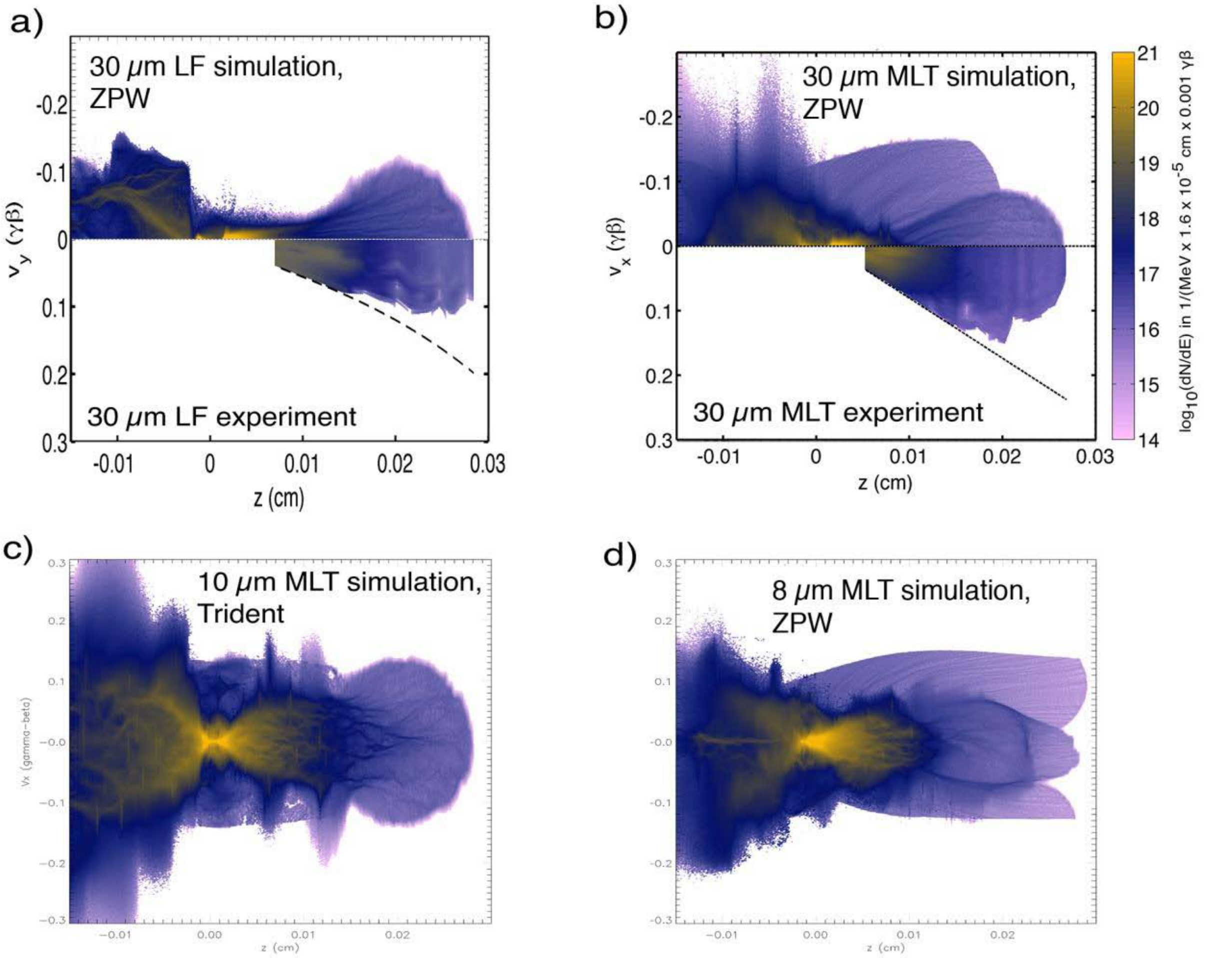

**Figure 30: Transverse phase space vs. longitudinal position.** *a) compares the phase space of a 30 μm LF between simulation and experiment, b) compares a 30 μm MLT. The laser enters from the left, expansion takes place in +z-direction. In both cases, there is a close agreement in beam envelope and particle density. Expanding preplasma in the MLT case causes the appearance of "wings" next to the main beam. c) shows a simulation for Trident, which has no ns prepulse and hence there are no wings in the profile. d) shows results for a 8 μm MLT using ZPW parameters. Here, the wings have higher energy than the main beam due to premature shockwave breakout.*

## 5.1. PREMATURE ELECTRON HEATING AND ITS IMPLICATION FOR PROTON ACCELERATION

The simulations indicate that the differences in proton beam properties between the targets and lasers are explained by a complex interplay of preplasma, prepulse a few ps prior to the main pulse, and the hot electron dynamics leading up to (and during) the main pulse.

Indeed, idealized simulations employing just a preplasma with double-exponential profile and Gaussian laser pulse (Figure 26, green lines) resulted in maximum proton energies of (160 ± 5) MeV, triple the measured values (54 ± 2.5 MeV) for a 15 µm thick MLT at ZPW. Furthermore, we could not reproduce an optimum MLT thickness for proton acceleration; instead the thinnest MLT always had the highest cutoff energies. Only the combined use of realistic preplasmas and ps-prepulses (-4.5 ps or earlier) resulted in the accurate recovery of the full suite of measured values mentioned.

The equality between 500 vs. 860 fs main pulse simulations for Trident (see Figure 27) provides further evidence that sub-ps variations are not the cause of the observations. MLT are more sensitive to the ps-prepulse than LF because of refluxing at early times. However, LF suffer from the non-Gaussian prepulse, too. Otherwise the measured LF-energies would be higher.

Accelerated preplasma also explains the differences in beam profile and divergence data between LF and MLT at ZPW. The expanding preplasma overlaps with the “main” beam from the target center, which can be clearly seen in the proton density plots in Figure 31. This causes the apparent knees in the divergence data, and also explains the fuzzy halos around the main beam. At Trident, additional proton sources for the MLT are the top and bottom edges of the target, which are partly accelerated in forward direction. For both lasers, the additional proton source results in a higher particle count for MLT vs. LF, which also explains the very high conversion efficiencies of over 10 %.

The dynamics of the hot electrons (represented by the average (per simulation grid cell) electron pressure, which is also known as the electron energy density) and protons (represented by their density) are shown in Figure 31 for a 15µm MLT at ZPW, and a 10 µm MLT at Trident. Both are compared to runs with idealized parameters. Here, idealized means that both the preplasma and laser pulse are approximated by analytical expressions. Laser injection direction, polarization, energy, etc. are kept unchanged. The laser pulse is Gaussian in time with 500 fs FWHM and no pre- or post-pulses. Aside from being inconsistent since a perfectly Gaussian laser pulse would not generate a preplasma, this idealized setup is how most computational work has been done to-date. In longitudinal direction (z-axis), the preplasma gradients were obtained by fitting a double-exponential curve to a 1D lineout of the HYDRA data at x = 0. In transverse direction (± x) the preplasma has no additional structure. Furthermore, the preplasma was assumed to consist of $Cu^{1+}$ and electrons only.

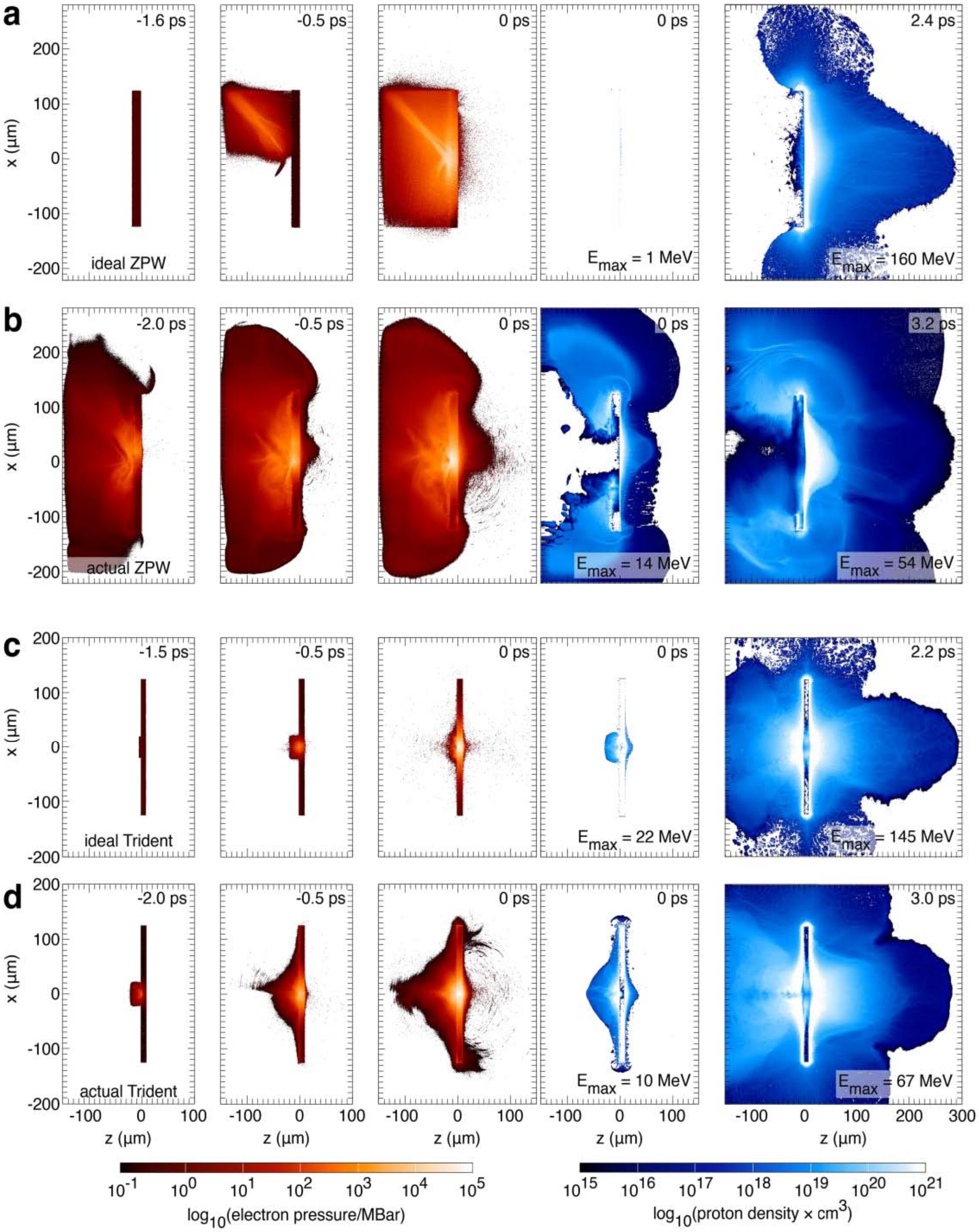

**Figure 31: Electron pressure and proton density vs. time.** ***a*** *shows the evolution of the electron pressure, which is a measure for the energy density, for an idealized, 2D PIC simulation. t = 0 ps denotes the time when the peak of the laser pulse reaches the front surface. For times greater equal zero the proton density distribution has been overlaid.* ***B*** *shows the same data using ZPW's prepulse data;* ***c*** *and* ***d*** *show simulations using Trident's prepulse data (****d****) or idealized (****c****). In contrast to the idealized simulations, both realistic cases show premature electron pressure (heating). This leads to premature proton beam expansion, as indicated by comparing the proton density plots at t = 0.*

Well before the peak reaches the target (t = -4 ps) there is already some significant electron pressure on the order of 200 MBar inside the target for the realistic runs. For later times, but still before the peak, electrons distribute largely in the preplasma. By the time the pressure starts to build up in the target in the idealized run (t = −0.5 ps), there is already significant rear-side expansion for the realistic MLT, which reduces the electric field that drives proton acceleration. By contrast, the idealized run has a larger area of high pressure at t = 0. Additionally, the idealized run shows a "channel" of higher pressure where the laser propagates. Here, MeV electrons can be generated by direct laser acceleration [90]. However, this channel is absent in the realistic runs due different density gradients (see the HYDRA simulations in Figure 29).

The simulations with Trident's prepulse (bottom rows) also show a significantly expanded target at t = 0. Overall, it performs closer to the ZPW MLT with prepulse than to the idealized ZPW MLT. Note that the ps-prepulse rise time was the only difference between the idealized and realistic Trident runs. Likewise, the two ideal cases (ZPW and Trident) both used the same ideal Gaussian pulse – with different preplasmas – and got basically the same result. These are two strong pieces of evidence that rise time matters more than the preplasma difference.

A comparison of the experimental and simulation results for 15 μm thick LF and MLT shows that both target types yield the same cutoff energy at ZPW (similarly, Trident shows the same cutoff energy for 1 μm targets). The simulations show that MLTs have more early acceleration and gradient weakening. However, MLTs get hotter from refluxing electrons during the main pulse than LF. Hence, even though premature expansion makes the MLTs accelerate earlier (and so one would expect a lower proton cutoff energy compared to LF), the MLTs get hotter during the main pulse and make up for the extra early expansion. Eventually, MLTs and LFs generate about the same at maximum proton energy. A similar trend is observed for Trident, but for thinner targets (1 and 10 μm vs. 15 and 25 μm at ZPW).

These observations explain the optimum MLT thickness. A too-thin target (LF or MLT) experiences a premature density gradient at the rear side. At peak time, the electric field in the rear-side sheath is then reduced [77], which leads to a lower-than-expected proton cutoff energy. Additionally, the expanding preplasma increases the target volume in which the fast electrons propagate and in which they can lose their energy. Too-thick targets do not develop a density gradient at the rear surface during the rising edge of the pulse. MLT can still somewhat confine the fast electrons, which leads to a slightly higher cutoff energy than for LF. MLT with the optimum thickness just balance the detrimental effect of the premature density gradient and the benefit of transverse refluxing or confinement of hot electrons, which keeps up the electron pressure and which drives proton acceleration.

The results also explain the higher shot-to-shot variations for MLT. Each laser shot has a slightly different spectrum due to fluctuations in the pump lasers, spectral noise etc. The width and shape of the spectrum is correlated to the temporal width and shape via the time-bandwidth product. Thus any spectral fluctuation results in a contrast variation or ps-prepulse variation. MLT are more sensitive to the prepulse due to the fine balance between premature density gradient and electron confinement, which results in larger shot-to-shot variations.

These data attest that the acceleration history during the run up phase just prior to peak laser field is important. We very clearly see that the realistic prepulse from -11.5 to -1 ps, and especially the last -4 ps to -1 ps, is making a large difference in the measurables such as proton emission. The results illustrate that the use of idealized prepulse, preplasma, and main pulse models, even for high-contrast HEDP lasers such as Trident, may not quantitatively agree with all experimental data. Thus, idealized treatments lead to a wrong interpretation of data. In a broader sense, exploring generalized scaling laws with only an irradiance dependency, e.g. for ion acceleration [22,24,79,80,91], electron temperature [92,93], or electron transport angles [94] will be further complicated since each laser system has a unique prepulse contrast and therefore a unique hot electron energy density history. Finally, our results explain why proton acceleration by Target Normal Sheath Acceleration (TNSA) – in contrast to predictions from scaling laws and idealized PIC simulations citations – has been limited to about 60 MeV for over a decade now. The highest proton energies to-date have been measured during this LDRD project. Our results show that real HEDP lasers are far from being Gaussian, even Trident which has the world's current best contrast for a 100J-class laser, resulting in premature target expansion which is detrimental for ion acceleration and which is shown to result in about 60 MeV cutoff energies. Hence, an enhancement of cutoff energies requires not only higher laser energies and intensities; it also requires a much better temporal contrast to suppress premature expansion. At this point, it will become questionable if TNSA with no other methods to improve the ps-prepulse rise time seen at the target is the best acceleration mechanism or if other proposed concepts such as volume acceleration [95-97] or radiation pressure acceleration [98-101] will be more favorable.

# 6. ENHANCEMENT OF LASER-DRIVEN ELECTRON ACCELERATION IN EXTENDED PREPLASMA

The previous sections have shown that key to optimize ion acceleration is a thorough understanding of electron dynamics both in the preplasma and the bulk of the target. While our computer simulations were able to reproduce the experimental data in great detail, they can be seen as "numerical experiments" since the simulation does not test a specific theory or assumption. Even seemingly simple observations, such as the existence of tens of MeV protons and therefore the existence of tens of MeV electrons, are difficult to explain without a solid theoretical model. Electrons with several ten MeV have energy well above the ponderomotive potential, which is on the order of 5 MeV for ZPW and Trident.

Simulations show that high-energy electrons are created both at the critical density surface where the laser gets reflected, and in the preplasma. The HYDRA simulations in the previous section have shown that ZPW exhibits a substantial preplasma, extending many wavelengths from the target surface along the beam path. The main pulse then interacts with this low-density plasma before reaching the target. It is important to understand if such interactions can generate hot electrons in addition to the ones produced at the critical surface [7,102].

The problem of high-energy electron generation in preplasma had attracted the attention of Dr. Alexey Arefiev and Prof. Boris Breizmann from the University of Texas at Austin (TX). Specifically, the exisiting explanation of direct laser acceleration (DLA) of electrons in a long plasma channel by Pukhov *et al.* [103] seemed to be incomplete. Dr. Arefiev developed a new theoretical description to explain DLA, and found that a parametric instability can explain the high electron energies observed in simulations. The model might have applicability not only for laser interaction with solid targets, but for gas jet experiments [104-107] as well. The Principal Investigator (PI) of this LDRD project helped to develop the general motivation of the theory, its relevance to the subject, as well as to estimate its validity for real experimental conditions. The results have been published in Physical Review Letters (PRL) [90]; the reader is invited to consult the reference for more details about parametric amplification. It should be noted that this publication has stimulated another publication in PRL [108], which was published just recently. A follow-up and extension of the original work by Dr. Arefiev, Dr. V.N. Khudik (UT Austin) and the PI has been submitted this month.

This page intentionally left blank.

# 7. SUMMARY AND OUTLOOK

This LDRD project investigated the feasibility of laser-driven ion radiography or deflectometry at Sandia's Z-Accelerator. Shortpulse, laser-driven proton radiography using the Target Normal Sheath Acceleration mechanism has been developed about 10 years ago to diagnose transient electromagnetic fields and density structures in laser-driven HEDP experiments, which are characterized by small volumes and very short time scales. Charged particle radiography on Z would enable us to map the electromagnetic fields during a Z discharge with sub-ps temporal and micron-scale spatial resolution. However, the much larger overall volume and target debris in Z experiments pose significant challenges for charged particle radiography.

To generate a proton beam near the object of interest at Z it will be necessary to re-direct the ZPW laser beam close to the object inside Z's vacuum center section. This is commonly done with flat plasma mirrors (PM). A PM has a reflectivity between 30 % and 80%, which in combination with the large focal length of the Off-Axis Parabola (OAP) at Z might result in insufficient laser intensity to generate a high-energy proton beam. Development of ellipsoidal plasma mirrors (EPM) with built-in alignment markers has started. EPM have two focal spots, which allows de-magnifying a laser beam in one focal spot if it is focused by the OAP to the other focus. Due to this de-magnification the laser intensity on target improves significantly. Furthermore, de-magnification also reduces the pointing instability of the laser by the de-magnification factor. If needed, an aperture can be placed at the first focus to enhance debris protection of the OAP at Z.
Two alignment prototypes were diamond turned with very high precision (10 μm) by MPCL (Raytheon/Ktech). A kinematic holder with motorized, 6-axis translation stage was developed in-house. Motion control was realized with an innovative, multi-touch Graphical User Interface using a Tablet PC. Beam focusing tests using a cw HeNe laser were performed, and showed 3.3× de-magnification with good focal spot quality. Focusing and pointing stability tests using the un-amplified, pulsed beam of ZPW in the 100 TW vacuum chamber are pending. Further development of the EPM had to be stopped late CY 12, when Sandia's support for MPCL was terminated.

Radiation background tests at Z have been performed in a ride-along of a Lincoln series experiment. A set of radiochromic film (RCF) was placed inside the Compact Point-Projection System (C-Pops) detector. C-Pops was placed about 10 cm from the load, the front entrance was filtered with a combination of total 2 mm thick Al and 2 mm thick Kapton foils. The measured increase of background after the exposure was low, which indicates that the filter combination is suitable. 25 MeV protons are required to penetrate the filter stack; this sets the lower energy limit for a proton radiography/deflectometry experiment at Z. If the signals are too low for RCF, a single-particle detector such as CR-39 could be used instead.

A relativistic, single-particle tracking code has been developed to simulate some simplified experiments at Z. Tracking of sub-relativistic protons shows that ion beam radiography of an imploding liner is not possible due to large $B_\Theta$ field. This is likely to be true for wire arrays as well. Protons with 4.5 GeV would be required to perform an actual radiography of the $B_\Theta$-field of an imploding liner, which is out of reach for existing and near-future laser systems. However, proton deflectometry could be feasible to measure the fringe fields for magnetic flux compression experiments in the framework of Inertial Confinement Fusion at Z. Using electromagnetic field distributions from a simplified numerical model a working scenario was developed. Tracking protons with 30 MeV through the fringe field region shows that there will be two indicators when magnetic flux compression takes places: an additional shift of the beam direction due to the locally enhanced $B_z$-field, and a shearing of the beam profile.

Experiments were performed at the 100 TW target chamber of ZPW to further investigate the proton source, as well as at Trident at Los Alamos National Laboratories. ZPW (100 J, 0.5 ps, 6 µm focal spot) or Trident (80 J, 0.5 ps, 6 µm focal spot) irradiated thin Cu foils with different thicknesses. The foils had either mm-long sides (referred to as large area foils, LF) or 250 µm side length (referred to as mass-limited targets, MLT). Stacks of RCF were used to measure the proton beam originating at the rear surface. An unexpected scaling with target thickness was found for the MLT. In contrast to LF, which yielded the highest proton energies for the thinnest foils, MLT exhibit an optimum target thickness that is not at the thinnest possible thickness. For ZPW, this optimum MLT thickness is 25-30 µm (cf., the LF optimum thickness is 15 µm); for Trident the optimum MLT thickness is 10 µm (cf., the optimum LF are 1 µm thick). Simplified one- and two-dimensional numerical simulations could not reproduce the experimental results. Only after numerically simulating the experiment as close to reality as possible, and at full scale, the experimental data could be reproduced. Never before has a shortpulse laser experiment been numerically simulated with such fine attention to details and resolution. The ns preplasma of ZPW was simulated in 3D with HYDRA, here a very complex mesh was developed that is able to resolve the expansion of the 10 nm-thick water impurity layer as well as the sharp edges of the target. This simulation was followed by a >10 ps long, fully explicit, 2D particle-in-cell simulation with LSP. LSP needed to be modified to allow non-normal laser incidence, a new particle collision package was used to correctly resolve inter-particle collisions in the dense parts of the target for over 10 ps simulation time. Each LSP run required about one week computation time using 1024 CPUs at Sandia's TLCC and TLCC2 compute clusters.

These simulations reproduced all measurements (max. energy, beam profile, divergence, energy conversion efficiency scaling, phase spaces, etc.), which gives confidence in the simulation methodology. Not that there has also been quantitative agreement with $K_\alpha$ x-ray data on several laser systems, which will be discussed below. This work was partly funded by this LDRD project, and further supports the fact that we can explain all available data with one model.

The simulations show that laser-accelerated protons are very sensitive to the laser pulse contrast on the ps time scale. The ps-scale laser rising edge is more important than commonly thought. The measured proton beam parameters result from a complex interplay of preplasma, prepule, ps-rising edge and main pulse. This insight has implications for all high-energy shortpulse laser work, such as but not limited to ion acceleration, $K_\alpha$ x-ray generation, warm dense matter experiments, etc. It is planned to submit these results to a high-impact scientific journal.

The role of the preplasma in the generation of fast electrons by an about one ps long laser pulse has been further investigated. A new theoretical model for Direct Laser Acceleration has been developed, which identifies a parametric instability as the cause of MeV-scale electrons in the preplasma. The results of this study have been published in Physical Review Letters; a follow-up article has been submitted in September 2013.

Programmatic work in our Center may benefit from the findings of this LDRD as follows. The new simulation methodology is superior to any previous methods, as it quantitatively reproduces all measured data. In addition to proton data, the simulation framework has been used to reproduce Cu and Sn $K_\alpha$ data (yield, pulse duration, spatial distribution) from ZPW, Trident and the Multi-Terawatt (MTW) laser at the Laboratory for Laser Energetics, University of Rochester, NY. Future development of high-energy (above 10 keV) x-rays to probe Z experiments with backlighting, x-ray Thomson scattering or x-ray spectroscopy will benefit from this simulation capability.

Development of EPMs to re-direct the ZPW laser beam and for enhanced debris protection may become an essential piece for high-energy x-ray Thomson scattering (XRTS) to "characterize materials in WDM [warm dense matter] and extreme plasma conditions, improve the understanding of underlying physics, and advance predictive capability" [109]. Performing XRTS with a Z Dynamic Material Properties load requires focusing the laser on-axis at Z. The report by Bailey *et al.* [109] has shown that substantial damage to the laser optics can happen in this configuration. Protecting the valuable laser optics from this debris is of paramount importance. The long-pulse laser ZBL uses baffle plates and a transmissive debris shield. The latter one cannot be used to transmit a fully compressed, full-energy ZPW pulse due to B-integral concerns. Here, EPM might add the required additional protection to realize an XRTS experiment using ZPW as the driver.

Proton deflectometry was shown to be feasible to detect magnetic flux compression at Z. ICF program scientists have shown interest in proton deflectometry, it is conceivable that a prototype experiment might be developed within the next 2 years.

ZPW has substantial ns prepulse, which causes a large-scale preplasma. This preplasma prevents using very thin target foils, which are required for new, proposed ion acceleration schemes such as Radiation Pressure Acceleration or Break-Out Afterburner (the latter mechanism is also called volume acceleration). These new mechanisms are predicted to result in >100 MeV to GeV proton and heavy ion beams, which, if successfully generated, might be used to perform an ion radiography experiment at Z within a 15 year time frame. In the nearer future, within 5 to 10 years, an improved laser contrast is required to test a novel $K_\alpha$ x-ray generation mechanism based on volume acceleration of a thin target foil [110], as well as to generate an intense, directed fast neutron beam [111,112]. A directed neutron beam could be used to probe very dense samples at Z via neutron imaging or scattering, as well as to better characterize neutron diagnostics for Z.

This page intentionally left blank.

# 8. REFERENCES

[1] G. R. Bennett, D. B. Sinars, D. F. Wenger, M. E. Cuneo, R. G. Adams, W. J. Barnard, D. E. Beutler, R. A. Burr, D. V. Campbell, L. D. Claus, J. S. Foresi, D. W. Johnson, K. L. Keller, C. Lackey, G. T. Leifeste, L. A. McPherson, T. D. Mulville, K. A. Neely, P. K. Rambo, D. C. Rovang, L. E. Ruggles, J. L. Porter, W. W. Simpson, I. C. Smith, and C. S. Speas, Review of Scientific Instruments **77**, 10E322 (2006).

[2] C. L. Morris, N. S. P. King, K. Kwiatkowski, F. G. Mariam, F. E. Merrill, and A. Saunders, Rep. Prog. Phys. **76**, 046301 (2013).

[3] M. Borghesi, D. H. Campbell, A. Schiavi, M. G. Haines, O. Willi, A. J. MacKinnon, P. Patel, L. A. Gizzi, M. GALIMBERTI, R. J. Clarke, F. Pegoraro, H. Ruhl, and S. Bulanov, Phys. Plasmas **9**, 2214 (2002).

[4] E. Clark, K. Krushelnick, J. Davies, M. Zepf, M. Tatarakis, F. Beg, A. Machacek, P. Norreys, M. Santala, I. Watts, and A. Dangor, Phys. Rev. Lett **84**, 670 (2000).

[5] A. Maksimchuk, S. Gu, K. Flippo, D. Umstadter, and V. Y. Bychenkov, Phys. Rev. Lett **84**, 4108 (2000).

[6] R. A. Snavely, M. H. Key, S. P. Hatchett, T. E. Cowan, M. Roth, T. W. Phillips, M. A. Stoyer, E. A. Henry, T. C. Sangster, M. S. Singh, S. C. Wilks, A. MacKinnon, A. Offenberger, D. M. Pennington, K. Yasuike, A. B. Langdon, B. F. Lasinski, J. Johnson, M. D. Perry, and E. M. Campbell, Phys. Rev. Lett **85**, 2945 (2000).

[7] S. Wilks, W. Kruer, M. Tabak, and A. Langdon, Phys. Rev. Lett **69**, 1383 (1992).

[8] S. J. Gitomer, R. D. Jones, F. Begay, A. W. Ehler, J. F. Kephart, and R. Kristal, Physics of Fluids **29**, 2679 (1986).

[9] T. Ditmire, T. Donnelly, A. M. Rubenchik, R. W. Falcone, and M. D. Perry, Physical Review a (Atomic **53**, 3379 (1996).

[10] K. Krushelnick, E. L. Clark, Z. Najmudin, M. Salvati, M. I. K. Santala, M. Tatarakis, A. E. Dangor, V. Malka, D. Neely, R. Allott, and C. Danson, Phys. Rev. Lett **83**, 737 (1999).

[11] A. V. Kuznetsov, T. Z. Esirkepov, F. F. Kamenets, and S. V. Bulanov, Plasma Physics Reports **27**, 211 (2001).

[12] H. Habara, K. L. Lancaster, S. Karsch, C. D. Murphy, P. A. Norreys, R. G. Evans, M. Borghesi, L. Romagnani, M. Zepf, T. Norimatsu, Y. Toyama, R. Kodama, J. A. King, R. Snavely, K. Akli, B. Zhang, R. Freeman, S. Hatchett, A. J. MacKinnon, P. Patel, M. H. Key, C. Stoeckl, R. B. Stephens, R. A. Fonseca, and L. O. Silva, Phys. Rev. E **70**, 46414 (2004).

[13] J. Badziak, S. Glowacz, S. Jablonski, P. Parys, J. Wolowski, H. Hora, J. Krása, L. Láska, and K. Rohlena, Plasma Phys. Control. Fusion **46**, 541 (2004).

[14] A. P. L. Robinson, M. Zepf, S. Kar, R. G. Evans, and C. Bellei, New J. Phys. **10**, 013021 (2008).

[15] L. Yin, B. J. Albright, B. M. Hegelich, and J. C. Fernández, Laser Part. Beams **24**, 291 (2006).

[16] T. Esirkepov, M. Borghesi, S. V. Bulanov, G. Mourou, and T. Tajima, Phys. Rev. Lett **92**, 175003 (2004).

[17] S. C. Wilks, A. B. Langdon, T. E. Cowan, M. Roth, M. Singh, S. Hatchett, M. H. Key, D. Pennington, A. MacKinnon, and R. A. Snavely, Phys. Plasmas **8**, 542 (2001).

[18] F. Nürnberg, M. Schollmeier, E. Brambrink, A. Blažević, D. C. Carroll, K. Flippo, D. C. Gautier, M. Geißel, K. Harres, B. M. Hegelich, O. Lundh, K. Markey, P. McKenna, D. Neely, J. Schreiber, and M. Roth, Review of Scientific Instruments **80**, 033301 (2009).

[19] T. E. Cowan, J. Fuchs, H. Ruhl, Y. Sentoku, A. Kemp, P. Audebert, M. Roth, R. Stephens, I. Barton, A. Blazevic, E. Brambrink, J. Cobble, J. C. Fernández, J.-C. Gauthier, M. Geissel, M. Hegelich, J. Kaae, S. Karsch, G. P. Le Sage, S. Letzring, M. Manclossi, S. Meyroneinc, A. Newkirk, H. Pépin, and N. Renard-Legalloudec, Nucl. Instrum. and Meth. A **544**, 277 (2005).

[20] T. E. Cowan, J. Fuchs, H. Ruhl, A. Kemp, P. Audebert, M. Roth, R. Stephens, I. Barton, A. Blazevic, E. Brambrink, J. Cobble, J. Fernández, J.-C. Gauthier, M. Geissel, M. Hegelich, J. Kaae, S. Karsch, G. P. Le Sage, S. Letzring, M. Manclossi, S. Meyroneinc, A. Newkirk, H. Pépin, and N. Renard-Legalloudec, Phys. Rev. Lett **92**, 204801 (2004).

[21] K. Flippo, T. Bartal, F. Beg, S. Chawla, J. Cobble, S. Gaillard, D. Hey, A. Mackinnon, A. MacPhee, P. Nilson, D. Offermann, S. Le Pape, and M. J. Schmitt, J. Phys.: Conf. Ser. **244**, 2033 (2010).

[22] J. Fuchs, P. Antici, E. D'Humières, E. Lefebvre, M. Borghesi, E. Brambrink, C. A. Cecchetti, M. Kaluza, V. Malka, M. Manclossi, S. Meyroneinc, P. Mora, J. Schreiber, T. Toncian, H. Pépin, and P. Audebert, Nature Phys. **2**, 48 (2006).

[23] D. T. Offermann, K. A. Flippo, J. Cobble, M. J. Schmitt, S. A. Gaillard, T. Bartal, D. V. Rose, D. R. Welch, M. Geissel, and M. Schollmeier, Phys. Plasmas **18**, 056713 (2011).

[24] L. Robson, P. T. Simpson, R. J. Clarke, K. W. D. Ledingham, F. Lindau, O. Lundh, T. Mccanny, P. Mora, D. Neely, C.-G. Wahlström, M. Zepf, and P. McKenna, Nature Phys. **3**, 58 (2007).

[25] M. Borghesi, A. Schiavi, D. H. Campbell, M. G. Haines, O. Willi, A. J. MacKinnon, L. A. Gizzi, M. GALIMBERTI, R. J. Clarke, and H. Ruhl, Plasma Phys. Control. Fusion **43**, 267 (2001).

[26] M. Borghesi, A. Schiavi, D. H. Campbell, M. G. Haines, O. Willi, A. J. MacKinnon, P. Patel, M. GALIMBERTI, and L. A. Gizzi, Review of Scientific Instruments **74**, 1688 (2003).

[27] S. Kar, M. Borghesi, C. A. Cecchetti, L. Romagnani, F. Ceccherini, T. V. Liseykina, A. Macchi, R. Jung, J. Osterholz, O. Willi, L. A. Gizzi, A. Schiavi, M. GALIMBERTI, and R. Heathcote, New J. Phys. **9**, 402 (2007).

[28] L. Romagnani, J. Fuchs, M. Borghesi, P. Antici, P. Audebert, F. Ceccherini, T. Cowan, T. Grismayer, S. Kar, A. Macchi, P. Mora, G. Pretzler, A. Schiavi, T. Toncian, and O. Willi, Phys. Rev. Lett **95**, 195001 (2005).

[29] K. Quinn, P. A. Wilson, C. A. Cecchetti, B. Ramakrishna, L. Romagnani, G. Sarri, L. Lancia, J. Fuchs, A. Pipahl, T. Toncian, O. Willi, R. J. Clarke, D. Neely, M. Notley, P. Gallegos, D. C. Carroll, M. N. Quinn, X. H. Yuan, P. McKenna, T. V. Liseykina, A. Macchi, and M. Borghesi, Phys. Rev. Lett **102**, 194801 (2009).

[30] K. Quinn, L. Romagnani, B. Ramakrishna, G. Sarri, M. Dieckmann, P. Wilson, J. Fuchs, L. Lancia, A. Pipahl, T. Toncian, O. Willi, R. Clarke, M. Notley, A. Macchi, and M. Borghesi, Phys. Rev. Lett **108**, 135001 (2012).

[31] A. Ravasio, L. Romagnani, S. Le Pape, A. Benuzzi-Mounaix, C. Cecchetti, D. Batani,

T. Boehly, M. Borghesi, R. Dezulian, L. Gremillet, E. Henry, D. Hicks, B. Loupias, A. MacKinnon, N. Ozaki, H. S. Park, P. Patel, A. Schiavi, T. Vinci, R. Clarke, M. Notley, S. Bandyopadhyay, and M. Koenig, Phys. Rev. E **82**, 16407 (2010).

[32] N. L. Kugland, D. D. Ryutov, P. Y. Chang, R. P. Drake, G. Fiksel, D. H. Froula, S. H. Glenzer, G. Gregori, M. Grosskopf, M. Koenig, Y. Kuramitsu, C. Kuranz, M. C. Levy, E. Liang, J. Meinecke, F. Miniati, T. Morita, A. Pelka, C. Plechaty, R. Presura, A. Ravasio, B. A. Remington, B. Reville, J. S. Ross, Y. Sakawa, A. Spitkovsky, H. Takabe, and H.-S. Park, Nat Phys **8**, 809 (2012).

[33] A. J. MacKinnon, P. K. Patel, D. W. Price, D. Hicks, L. Romagnani, and M. Borghesi, Appl. Phys. Lett. **82**, 3188 (2003).

[34] A. J. MacKinnon, P. K. Patel, M. Borghesi, R. C. Clarke, R. R. Freeman, H. Habara, S. P. Hatchett, D. Hey, D. G. Hicks, S. Kar, M. H. Key, J. A. King, K. Lancaster, D. Neely, A. Nikkro, P. A. Norreys, M. M. Notley, T. W. Phillips, L. Romagnani, R. A. Snavely, R. B. Stephens, and R. P. J. Town, Phys. Rev. Lett **97**, 045001 (2006).

[35] M. Borghesi, S. V. Bulanov, T. Z. Esirkepov, S. Fritzler, S. Kar, T. V. Liseikina, V. Malka, F. Pegoraro, L. Romagnani, J. P. Rousseau, A. Schiavi, O. Willi, and A. V. Zayats, Phys. Rev. Lett **94**, 195003 (2005).

[36] L. Willingale, P. M. Nilson, M. C. Kaluza, A. E. Dangor, R. G. Evans, P. Fernandes, M. G. Haines, C. Kamperidis, R. J. Kingham, C. P. Ridgers, M. Sherlock, A. G. R. Thomas, M. S. Wei, Z. Najmudin, K. Krushelnick, S. Bandyopadhyay, M. Notley, S. Minardi, M. Tatarakis, and W. Rozmus, Phys. Plasmas **17**, 043104 (2010).

[37] D. T. Offermann, K. A. Flippo, S. A. Gaillard, D. C. Gautier, S. Letzring, J. C. Cobble, G. Wurden, R. P. Johnson, T. Shimada, D. S. Montgomery, R. P. Gonzales, T. Hurry, F. Archuleta, M. J. Schmitt, S.-M. Reid, T. Bartal, M. S. Wei, D. P. Higginson, F. N. Beg, M. Geissel, and M. Schollmeier, J. Phys.: Conf. Ser. **244**, 2053 (2010).

[38] M. J. E. Manuel, N. Sinenian, F. H. Séguin, C. K. Li, J. A. Frenje, H. G. Rinderknecht, D. T. Casey, A. B. Zylstra, R. D. Petrasso, and F. N. Beg, Appl. Phys. Lett. **100**, 203505 (2012).

[39] O. Gotchev, P. Chang, J. Knauer, D. Meyerhofer, O. Polomarov, J. Frenje, C. Li, M. Manuel, R. Petrasso, J. Rygg, F. Séguin, and R. Betti, Phys. Rev. Lett **103**, 215004 (2009).

[40] S. A. Slutz, M. C. Herrmann, R. A. Vesey, A. B. Sefkow, D. B. Sinars, D. C. Rovang, K. J. Peterson, and M. E. Cuneo, Phys. Plasmas **17**, 056303 (2010).

[41] J. Schwarz, P. Rambo, M. Kimmel, M. Geissel, G. Robertson, M. Ramsey, D. Headley, and B. Atherton, Phys. Rev. ST Accel. Beams **13**, 041001 (2010).

[42] C. Thaury, F. Quéré, J.-P. Geindre, A. Levy, T. Ceccotti, P. Monot, M. Bougeard, F. Réau, P. D'Oliveira, P. Audebert, R. Marjoribanks, and P. Martin, Nat Phys **3**, 424 (2007).

[43] M. Geissel, M. S. Schollmeier, M. W. Kimmel, P. K. Rambo, J. Schwarz, B. W. Atherton, and E. Brambrink, Review of Scientific Instruments **82**, 053101 (2011).

[44] M. Nakatsutsumi, A. Kon, S. Buffechoux, P. Audebert, J. Fuchs, and R. Kodama, Optics Letters **35**, 2314 (2010).

[45] A. Kon, M. Nakatsutsumi, S. Buffechoux, Z. L. Chen, J. Fuchs, Z. Jin, and R. Kodama, J. Phys.: Conf. Ser. **244**, 2008 (2010).

[46] R. McBride, S. Slutz, C. Jennings, D. Sinars, M. Cuneo, M. Herrmann, R. Lemke, M. Martin, R. Vesey, K. Peterson, A. Sefkow, C. Nakhleh, B. Blue, K. Killebrew, D.

Schroen, T. Rogers, A. Laspe, M. Lopez, I. Smith, B. Atherton, M. Savage, W. Stygar, and J. Porter, Phys. Rev. Lett **109**, 135004 (2012).

[47] S. Gaillard, J. Fuchs, N. Renard-Le Galloudec, and T. E. Cowan, Review of Scientific Instruments **78**, 013304 (2007).

[48] C. K. Birdsall and A. B. Langdon, *Plasma Physics via Computer Simulations*, 1st ed. (Taylor & Francis, New York, 2004).

[49] F. L. Zheng, S. Z. Wu, H.-C. Wu, C. T. Zhou, H. B. Cai, M. Y. Yu, T. Tajima, X. Q. Yan, and X. T. He, Phys. Plasmas **20**, 013107 (2013).

[50] P. McKenna, F. Lindau, O. Lundh, D. C. Carroll, R. J. Clarke, K. W. D. Ledingham, T. Mccanny, D. Neely, A. P. L. Robinson, L. Robson, P. T. Simpson, C.-G. Wahlström, and M. Zepf, Plasma Phys. Control. Fusion **49**, 223 (2007).

[51] B. M. Hegelich, B. Albright, P. Audebert, A. Blazevic, E. Brambrink, J. Cobble, T. Cowan, J. Fuchs, J. C. Gauthier, C. Gautier, M. Geissel, D. Habs, R. Johnson, S. Karsch, A. Kemp, S. Letzring, M. Roth, U. Schramm, J. Schreiber, K. J. Witte, and J. C. Fernández, Phys. Plasmas **12**, 6314 (2005).

[52] E. Esarey, C. B. Schroeder, and W. P. Leemans, Reviews of Modern Physics **81**, 1229 (2009).

[53] J. C. Fernández, B. Hegelich, J. Cobble, K. Flippo, S. Letzring, R. Johnson, D. Gautier, T. Shimada, G. A. Kyrala, Y. Wang, C. J. Wetteland, and J. Schreiber, Laser Part. Beams **23**, 267 (2005).

[54] G. Hoffmeister, C. Bellei, K. Harres, D. Ivanov, D. Kraus, A. Pelka, B. Rethfeld, G. Schaumann, and M. Roth, Phys. Rev. ST Accel. Beams **16**, 041304 (2013).

[55] A. Diaw and P. Mora, Phys. Rev. E **86**, 026403 (2012).

[56] H. Schmitz, Phys. Plasmas **19**, 083115 (2012).

[57] J. Fuchs, T. E. Cowan, P. Audebert, H. Ruhl, L. Gremillet, A. Kemp, M. Allen, A. Blazevic, J.-C. Gauthier, M. Geissel, M. Hegelich, S. Karsch, P. Parks, M. Roth, Y. Sentoku, R. Stephens, and E. M. Campbell, Phys. Rev. Lett **91**, 255002 (2003).

[58] P. McKenna, A. Robinson, D. Neely, M. Desjarlais, D. Carroll, M. Quinn, X. Yuan, C. Brenner, M. Burza, M. Coury, P. Gallegos, R. Gray, K. Lancaster, Y. Li, X. Lin, O. Tresca, and C.-G. Wahlström, Phys. Rev. Lett **106**, (2011).

[59] Y. Sentoku, E. D'Humières, L. Romagnani, P. Audebert, and J. Fuchs, Phys. Rev. Lett **107**, (2011).

[60] K. Zeil, J. Metzkes, T. Kluge, M. Bussmann, T. E. Cowan, S. D. Kraft, R. Sauerbrey, and U. Schramm, Nature Communications **3**, 874 (2012).

[61] T. Nakamura, K. Mima, S. Ter-Avetisyan, M. Schnürer, T. Sokollik, P. V. Nickles, and W. Sandner, Phys. Rev. E **77**, 36407 (2008).

[62] T. Bartal, M. E. Foord, C. Bellei, M. H. Key, K. A. Flippo, S. A. Gaillard, D. T. Offermann, P. K. Patel, L. C. Jarrott, D. P. Higginson, M. Roth, A. Otten, D. Kraus, R. B. Stephens, H. S. McLean, E. M. Giraldez, M. S. Wei, D. C. Gautier, and F. N. Beg, Nat Phys **7**, 1 (2011).

[63] O. Tresca, D. C. Carroll, X. H. Yuan, B. Aurand, V. Bagnoud, C. M. Brenner, M. Coury, J. Fils, R. J. Gray, T. Kuhl, C. Li, Y. T. Li, X. X. Lin, M. N. Quinn, R. G. Evans, B. Zielbauer, M. Roth, D. Neely, and P. McKenna, Plasma Phys. Control. Fusion **53**, 105008 (2011).

[64] S. Buffechoux, J. Psikal, M. Nakatsutsumi, L. Romagnani, A. Andreev, K. Zeil, M. Amin, P. Antici, T. Burris-Mog, A. Compant-La-Fontaine, E. D humières, S.

Fourmaux, S. Gaillard, F. Gobet, F. Hannachi, S. Kraft, A. Mancic, C. Plaisir, G. Sarri, M. Tarisien, T. Toncian, U. Schramm, M. Tampo, P. Audebert, O. Willi, T. Cowan, H. Pépin, V. Tikhonchuk, M. Borghesi, and J. Fuchs, Phys. Rev. Lett **105**, 015005 (2010).
[65] T. Toncian, M. Swantusch, M. Toncian, O. Willi, A. A. Andreev, and K. Y. Platonov, Phys. Plasmas **18**, 043105 (2011).
[66] T. Sokollik, T. Paasch-Colberg, K. Gorling, U. Eichmann, M. Schnürer, S. Steinke, P. V. Nickles, A. Andreev, and W. Sandner, New J. Phys. **12**, 3013 (2010).
[67] T. Kluge, W. Enghardt, S. D. Kraft, U. Schramm, K. Zeil, T. E. Cowan, and M. Bussmann, Phys. Plasmas **17**, 123103 (2010).
[68] J. Psikal, V. T. Tikhonchuk, J. Limpouch, and O. Klimo, Phys. Plasmas **17**, 3102 (2010).
[69] M. Burza, A. Gonoskov, G. Genoud, A. Persson, K. Svensson, M. Quinn, P. McKenna, M. Marklund, and C.-G. Wahlström, New J. Phys. **13**, 013030 (2011).
[70] J. Schwarz, P. Rambo, M. Geissel, A. Edens, I. Smith, E. Brambrink, M. Kimmel, and B. Atherton, J. Phys.: Conf. Ser. **112**, 032020 (2008).
[71] S. Palaniyappan, B. M. Hegelich, H.-C. Wu, D. Jung, D. C. Gautier, L. Yin, B. J. Albright, R. P. Johnson, T. Shimada, S. Letzring, D. T. Offermann, J. Ren, C. Huang, R. Hörlein, B. Dromey, J. C. Fernandez, and R. C. Shah, Nat Phys **8**, 1 (2012).
[72] D. S. Hey, M. H. Key, A. J. MacKinnon, A. G. Macphee, P. K. Patel, R. R. Freeman, L. D. van Woerkom, and C. M. Castaneda, Review of Scientific Instruments **79**, 3501 (2008).
[73] R. C. Shah, R. P. Johnson, T. Shimada, K. A. Flippo, J. C. Fernandez, and B. M. Hegelich, Optics Letters **34**, 2273 (2009).
[74] M. Roth, A. Blazevic, M. Geissel, T. Schlegel, T. E. Cowan, M. Allen, J.-C. Gauthier, P. Audebert, J. Fuchs, J. Meyer-Ter-Vehn, M. Hegelich, S. Karsch, and A. Pukhov, Phys. Rev. ST Accel. Beams **5**, 61301 (2002).
[75] T. Ditmire, E. T. Gumbrell, R. A. Smith, L. Mountford, and M. H. R. Hutchinson, Phys. Rev. Lett **77**, 498 (1996).
[76] D. Du, X. Liu, G. Korn, J. Squier, and G. Mourou, Appl. Phys. Lett. **64**, 3071 (1994).
[77] T. Grismayer and P. Mora, Phys. Plasmas **13**, 032103 (2006).
[78] J. Fuchs, C. A. Cecchetti, M. Borghesi, T. Grismayer, E. D'Humières, P. Antici, S. Atzeni, P. Mora, A. Pipahl, L. Romagnani, A. Schiavi, Y. Sentoku, T. Toncian, P. Audebert, and O. Willi, Phys. Rev. Lett **99**, 015002 (2007).
[79] J. Schreiber, F. Bell, F. Gruner, U. Schramm, M. Geissler, M. Schnürer, S. Ter-Avetisyan, B. M. Hegelich, J. Cobble, E. Brambrink, J. Fuchs, P. Audebert, and D. Habs, Phys. Rev. Lett **97**, 045005 (2006).
[80] M. Passoni, L. Bertagna, and A. Zani, New J. Phys. **12**, 5012 (2010).
[81] P. Mora, Phys. Rev. E **72**, 56401 (2005).
[82] T. P. Hughes, R. E. Clark, and S. S. Yu, Phys. Rev. ST Accel. Beams **2**, 110401 (1999).
[83] M. Bonitz, G. Bertsch, V. Filinov, and H. Ruhl, Cambridge University Press (2004).
[84] M. M. Marinak, G. D. Kerbel, N. A. Gentile, O. Jones, D. Munro, S. Pollaine, T. R. Dittrich, and S. W. Haan, Phys. Plasmas **8**, 2275 (2001).
[85] F. Brunel, Phys. Rev. Lett **59**, 52 (1987).
[86] W. Kruer and K. Estabrook, Physics of Fluids **28**, 430 (1985).
[87] C. D. Chen, A. J. Kemp, F. Perez, A. Link, F. N. Beg, S. Chawla, M. H. Key, H.

McLean, A. Morace, Y. Ping, A. Sorokovikova, R. B. Stephens, M. Streeter, B. Westover, and P. K. Patel, Phys. Plasmas **20**, 052703 (2013).
[88] A. V. Brantov, V. Y. Bychenkov, and V. Rozmus, Quantum Electronics **37**, 863 (2008).
[89] D. R. Welch, D. V. Rose, M. E. Cuneo, R. B. Campbell, and T. A. Mehlhorn, Phys. Plasmas **13**, 063105 (2006).
[90] A. Arefiev, B. Breizman, M. Schollmeier, and V. Khudik, Phys. Rev. Lett **108**, 145004 (2012).
[91] K. Zeil, S. D. Kraft, S. Bock, M. Bussmann, T. E. Cowan, T. Kluge, J. Metzkes, T. Richter, R. Sauerbrey, and U. Schramm, New J. Phys. **12**, 5015 (2010).
[92] P. Gibbon, *Short Pulse Laser Interactions with Matter: an Introduction* (Imperial College Press, London, UK, 2005).
[93] T. Tanimoto, H. Habara, R. Kodama, M. Nakatsutsumi, K. A. Tanaka, K. L. Lancaster, J. S. Green, R. H. H. Scott, M. Sherlock, P. A. Norreys, R. G. Evans, M. G. Haines, S. Kar, M. Zepf, J. King, T. Ma, M. S. Wei, T. Yabuuchi, F. N. Beg, M. H. Key, P. Nilson, R. B. Stephens, H. Azechi, K. Nagai, T. Norimatsu, K. Takeda, J. Valente, and J. R. Davies, Phys. Plasmas **16**, 2703 (2009).
[94] J. S. Green, V. M. Ovchinnikov, R. G. Evans, K. U. Akli, H. Azechi, F. N. Beg, C. Bellei, R. R. Freeman, H. Habara, R. Heathcote, M. H. Key, J. A. King, K. L. Lancaster, N. C. Lopes, T. Ma, A. J. MacKinnon, K. Markey, A. Mcphee, Z. Najmudin, P. Nilson, R. Onofrei, R. Stephens, K. Takeda, K. A. Tanaka, W. Theobald, T. Tanimoto, J. Waugh, L. van Woerkom, N. C. Woolsey, M. Zepf, J. R. Davies, and P. A. Norreys, Phys. Rev. Lett **100**, 15003 (2008).
[95] D. Jung, L. Yin, B. J. Albright, D. C. Gautier, S. Letzring, B. Dromey, M. Yeung, R. Hörlein, R. Shah, S. Palaniyappan, K. Allinger, J. Schreiber, K. J. Bowers, H.-C. Wu, J. C. Fernández, D. Habs, and B. M. Hegelich, New J. Phys. **15**, 023007 (2013).
[96] D. Jung, L. Yin, D. C. Gautier, H.-C. Wu, S. Letzring, B. Dromey, R. Shah, S. Palaniyappan, T. Shimada, R. P. Johnson, J. Schreiber, D. Habs, J. C. Fernández, B. M. Hegelich, and B. J. Albright, Phys. Plasmas **20**, 083103 (2013).
[97] L. Yin, B. Albright, K. Bowers, D. Jung, J. Fernández, and B. Hegelich, Phys. Rev. Lett **107**, (2011).
[98] B. Aurand, S. Kuschel, O. Jäckel, C. Rödel, H. Y. Zhao, S. Herzer, A. E. Paz, J. Bierbach, J. Polz, B. Elkin, G. G. Paulus, A. Karmakar, P. Gibbon, T. Kuehl, and M. C. Kaluza, New J. Phys. **15**, 033031 (2013).
[99] S. Kar, K. Kakolee, B. Qiao, A. Macchi, M. Cerchez, D. Doria, M. Geissler, P. McKenna, D. Neely, J. Osterholz, R. Prasad, K. Quinn, B. Ramakrishna, G. Sarri, O. Willi, X. Yuan, M. Zepf, and M. Borghesi, Phys. Rev. Lett **109**, 185006 (2012).
[100] B. Qiao, M. Geissler, S. Kar, M. Borghesi, and M. Zepf, Plasma Phys. Control. Fusion **53**, 124009 (2011).
[101] A. Henig, S. Steinke, M. Schnürer, T. Sokollik, R. Hörlein, D. Kiefer, D. Jung, J. Schreiber, B. Hegelich, X. Yan, J. Meyer-Ter-Vehn, T. Tajima, P. Nickles, W. Sandner, and D. Habs, Phys. Rev. Lett **103**, 245003 (2009).
[102] P. Mulser, S. M. Weng, and T. Liseykina, Phys. Plasmas **19**, 043301 (2012).
[103] A. Pukhov, Z. M. Sheng, and J. Meyer-Ter-Vehn, Phys. Plasmas **6**, 2847 (1999).
[104] C. Gahn, G. D. Tsakiris, G. Pretzler, K. J. Witte, P. Thirolf, D. Habs, C. Delfin, and C.-G. Wahlström, Phys. Plasmas **9**, 987 (2002).

[105] C. Gahn, G. D. Tsakiris, A. Pukhov, J. Meyer-Ter-Vehn, G. Pretzler, P. Thirolf, D. Habs, and K. J. Witte, Phys. Rev. Lett **83**, 4772 (1999).

[106] S. Kneip, S. R. Nagel, C. Bellei, N. Bourgeois, A. E. Dangor, A. Gopal, R. Heathcote, S. P. D. Mangles, J. R. Marquès, A. Maksimchuk, P. M. Nilson, K. T. Phuoc, S. Reed, M. Tzoufras, F. S. Tsung, L. Willingale, W. B. Mori, A. Rousse, K. Krushelnick, and Z. Najmudin, Phys. Rev. Lett **100**, 105006 (2008).

[107] S. Mangles, B. Walton, M. Tzoufras, Z. Najmudin, R. Clarke, A. Dangor, R. Evans, S. Fritzler, A. Gopal, C. Hernandez Gomez, W. Mori, W. Rozmus, M. Tatarakis, A. Thomas, F. Tsung, M. Wei, and K. Krushelnick, Phys. Rev. Lett **94**, 245001 (2005).

[108] A. P. L. Robinson, A. V. Arefiev, and D. Neely, Phys. Rev. Lett **111**, 065002 (2013).

[109] J. E. Bailey, T. Ao, E. Harding, S. B. Hansen, M. P. Desjarlais, R. W. Lemke, G. A. Rochau, J. Reneker, and D. Romero, *X-Ray Thomson Scattering Measurements of Warm Dense Matter* (Sandia National Laboratories, Albuquerque, 2012), pp. 1–103.

[110] A. Sefkow, G. Bennett, M. Geissel, M. Schollmeier, B. Franke, and B. Atherton, Phys. Rev. Lett **106**, (2011).

[111] M. Roth, D. Jung, K. Falk, N. Guler, O. Deppert, M. Devlin, A. Favalli, J. Fernández, D. Gautier, M. Geissel, R. Haight, C. Hamilton, B. Hegelich, R. Johnson, F. Merrill, G. Schaumann, K. Schoenberg, M. Schollmeier, T. Shimada, T. Taddeucci, J. Tybo, F. Wagner, S. Wender, C. Wilde, and G. Wurden, Phys. Rev. Lett **110**, 044802 (2013).

[112] D. Jung, K. Falk, N. Guler, O. Deppert, M. Devlin, A. Favalli, J. C. Fernández, D. C. Gautier, M. Geissel, R. Haight, C. E. Hamilton, B. M. Hegelich, R. P. Johnson, F. Merrill, G. Schaumann, K. Schoenberg, M. Schollmeier, T. Shimada, T. Taddeucci, J. L. Tybo, S. A. Wender, C. H. Wilde, G. A. Wurden, and M. Roth, Phys. Plasmas **20**, 056706 (2013).

This page intentionally left blank.

# DISTRIBUTION

1 The University of Texas at Austin
Attn: A.V. Arefiev
Institute for Fusion Studies (RLM 11.312)
2515 Speedway C1500
Austin, TX 78712-1203

1 Los Alamos National Laboratory
Attn: K.A. Flippo
P.O. Box 1663, Mailstop F606
Los Alamos, New Mexico 87545

| | | | |
|---|---|---|---|
| 1 | MS1186 | A.B. Sefkow | 1684 |
| 1 | MS1189 | D.G. Flicker | 1646 |
| 1 | MS1190 | G.A. Rochau | 1675 |
| 1 | MS1193 | M.E. Cuneo | 1650 |
| 5 | MS1193 | M.S. Schollmeier | 1682 |
| 1 | MS1193 | R.D. McBride | 1688 |
| 1 | MS1193 | M. Geissel | 1682 |
| 1 | MS1193 | J.L. Porter | 1682 |
| 1 | MS1193 | P.K. Rambo | 1682 |
| 1 | MS1193 | D.B. Sinars | 1688 |
| 1 | MS1193 | J. Schwarz | 1682 |
| 1 | MS1218 | B.W. Atherton | 5944 |
| 1 | MS0899 | Technical Library | 9536 (electronic copy) |
| 1 | MS0359 | D. Chavez, LDRD Office | 1911 |

Sandia National Laboratories